

# Radio Positioning with EM Processing of the Spherical Wavefront

Francesco Guidi *Member, IEEE*, and Davide Dardari *Senior, IEEE*

## Abstract

Next 5G and beyond applications have attracted a tremendous interest towards systems using antenna arrays with an extremely large number of antennas where the technology conceived for communication might also be exploited for high-accuracy positioning applications. In this paper we investigate the possibility to infer the position of a single antenna transmitter using a single asynchronous receiving node by retrieving information from the incident spherical wavefront. To this end, we consider the adoption of a suitable mix of processing at electromagnetic (EM) and signal levels, as a lower complexity alternative to classical massive array systems where the processing is done entirely at signal level. Thus, we first introduce a dedicated general model for different EM processing architectures, and successively we investigate the attainable positioning performance according to the use or not of a lens that can have either a reconfigurable or a fixed phase profile. The effect of the interference is also investigated to evaluate the robustness of the considered system to the presence of multiple simultaneous transmitting sources. Results, obtained for different apertures of the exploited lens/array, confirm the possibility to achieve interesting positioning performance using a single antenna array with limited aperture.

## Index Terms

Spherical Wavefront, Near-Field, Holographic Positioning, Massive Array, Lens Array, mm-wave

F. Guidi is with the National Research Council (CNR) of Italy, Institute of Electronics, Computer and Telecommunication Engineering (IEIIT), via del Risorgimento 2, 40136 Bologna, Italy.

D. Dardari is with the Department of Electrical, Electronic, and Information Engineering “Guglielmo Marconi” - DEI, University of Bologna, Via Venezia 52, 47521 Cesena, ITALY. (e-mail: francesco.guidi@ieiit.cnr.it, davide.dardari@unibo.it).

The work has been partially funded by the European Commission under H2020 project XCYCLE (grant nr. 635975). This is also part of ATTRACT that has received funding from the European Union’s Horizon 2020 Research and Innovation Programme.

## I. INTRODUCTION

Indoor positioning systems have attracted a great interest in a large variety of scenarios because of the possibility of performing high accuracy users' localization even when Global Navigation Satellite System (GNSS) signal is not available and alternative positioning systems are required [1]–[3]. Currently, there is a large variety of ad-hoc solutions for indoor localization and tracking [4]–[7], spanning from the systems based on ultrasounds or to more recent impulse radio UWB (IR-UWB) techniques [6], [8]–[10]. Unfortunately, most of such solutions require that a mobile node is detected at least from three reference nodes (multiple anchor nodes) located in known positions, with the need to realize ad-hoc and often redundant infrastructures that might become not convenient in many indoor scenarios. Consequently, it would be of great help if the networks deployed for communication could be also used for indoor localization, but such networks usually consist of a single access point designed to guarantee single-anchor coverage.

In this context, next sixth generation (6G) mobile wireless networks will introduce new technologies based on the massive deployment of antennas into small areas, allowing to boost not only communication but also single-anchor localization capabilities at an unprecedented scale of accuracy [11]–[17]. In general, direct positioning approaches with single antenna arrays provide better performance than two-step localization algorithms as the latter may be suboptimal according to the data processing inequality [18]–[20]. Nevertheless, traditional two-step localization algorithms, based on the estimation of intermediate quantities such as angle-of-arrival (AOA) and time-of-arrival (TOA), are often implemented in practice as they are more pragmatic and less complex [21]–[26]. As an example, both ESPRIT and MUSIC-based approaches have been widely proposed for AOA estimate [27]. Unfortunately, such solutions require multiple interactions between transmitter and receiver as well as an extremely precise system synchronization [28], which could reduce the available bandwidth for communication and make the system still costly, especially if addressed to Internet of Things (IoT) applications.

A possible alternative solution is to infer the transmitter position from the spherical wavefront associated to the signal transmitted by the mobile node (source), which is possible in all those situations where the wavefront curvature is significant with respect to the antenna aperture in relation to the wavelength. In fact, while in far-field propagation regime the wavefront is plane and only the AOA information can be inferred using an antenna array, when operating in near-field regime (Fresnel region) the wavefront tends to be spherical and also the distance information,

e.g. the position, can be inferred from it.

This concept is not new, and it has been widely exploited for acoustic waves [29], [30] or at microwaves only considering very short distances or using very large (often not practical) antennas [31]. In [32], the curvature information has been exploited, with a moving source approaching to the receiver so that, entering in the Fresnel region, the incoming wave cannot be regarded as plane anymore. For instance, in [33], an approach using multi-tone signalling and multi-arrays is described, whereas in [34], a MUSIC-based method is proposed and an extensive analysis on the attainable fundamental localization limits is derived in near-field propagation conditions [35]. In addition, other previous works apply the Fresnel approximation to arrays with special geometries, e.g. uniform linear arrays [36]–[39], and account for the model mismatch while evaluating the positioning performance [40].

With the advent of millimeter-waves (mm-wave)-based solutions, direct positioning is in principle possible even with antenna arrays with limited aperture [41] or by the exploitation of distributed architectures [42], [43]. However, this requires the presence of a huge amount of antenna elements, each connected to a RF chain, which could lead to an extremely complex receiver, as they usually contain several electronic components, such as analog to digital converters (ADC), mixers, local oscillators etc. [44].

A way to reduce the complexity is by performing some (pre-)processing of the incident wavefront directly at electromagnetic (EM) level through the introduction of EM lens, as fostered by the advent of next 6G [45]. Such EM lenses can be either reconfigurable, namely reconfigurable lens (R-lens), or not, namely non-reconfigurable lens (NR-lens). According to NR-lens, recent studies have investigated the possibility to exploit EM lens-based massive arrays operating at mm-wave as a promising solution for drastically reducing the overall system complexity [46]. NR-lens can be implemented with different techniques, either including dielectric materials with ad-hoc designed surfaces (e.g., convex lenses), or antenna arrays or sub-wavelength spatial phase shifters [46], [47]. By adopting a lens to collimate the beams in precise directions, it is possible to spatially discriminate signals in the analog domain [46], [48], [49]. Consequently, thanks to the lens, there is a unique relation between the incident and the output angles of the impinging and refracted waves, respectively. This operation allows reducing the number of antennas with respect to traditional massive arrays, and to move from discrete beamforming architectures towards continuous-aperture phased arrays. Indeed, the use of such lenses has already been investigated only in far-field [46], [48], [49], and their performance has not yet been characterized in the

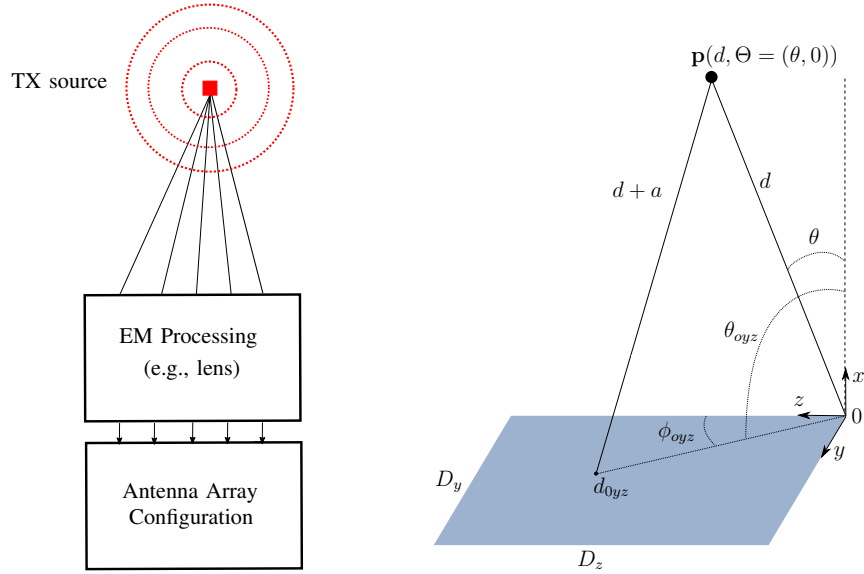


Fig. 1: Left: general scheme composed of the EM processing scheme that focuses the incident wave towards the antenna array. Right: incident wavefront on the EM processing surface.

Fresnel region.

In addition, while NR-lenses are passive and thus not reconfigurable, R-lens based solutions are programmable in real-time. In this sense, 6G solutions are moving towards the realization of holographic phase profiles, or of reconfigurable intelligent surfaces (RISs), to put in place a programmable smart radio environment [50]–[56]. According to this vision, metamaterials represent an important and recent solution for the realization of R-lens [57] thanks to the possibility to achieve a flexible control of the EM wavefront [58]–[60] while guaranteeing, whenever required, compact size [61], [62]. Other interesting opportunities account for the execution of mathematical operations with layers of metamaterials [63], the realization of electronically reconfigurable transmitarray [64], or reconfigurable reflectarray technology [65].

In this context, starting from our analysis in [49], [66], [67], here we investigate the radio positioning capabilities of a mm-wave source by introducing a generic architecture composed of an EM processing section, which can directly operate on the spherical wavefront, and of an array architecture that collects the impinging signal, as shown in Fig. 1.<sup>1</sup> More specifically, differently from the state of the art, we first introduce a general model that entails the presence (if any) of an EM lens performing the processing at EM level before the antenna array. Successively,

<sup>1</sup>For the sake of simplicity, we assume that it holds  $\Theta = (\theta, 0)$ . The extension to  $\phi \neq 0$  is straightforward.

we compare different architectures according to the presence or absence of the lens, that can be either reconfigurable or not, and to the number of employed antennas. Such a trade-off is then investigated by analyzing the attainable positioning accuracy and interference rejection capability when the aperture is varied.

The main contributions of the manuscript can be summarized as follows.

- We provide a generalized framework for retrieving positioning information from the wavefront curvature when EM processing is performed prior the processing of signals at each antenna. Differently from [51], we propose a general framework that encompasses the kind of antenna array adopted with the add-on (if any) of an external lens capable to partially (or completely) perform the post-processing.
- We consider different practical schemes, employing or not the use of an EM lens. In particular, we investigate the effect on the positioning accuracy when the required processing is split between EM level, performed either by using R-lens or NR-lens, and signal level, i.e., processing the RF signal after an antenna element.
- We evaluate, through an extensive simulation analysis, the positioning performance, comprising a differential approach that might unburden the signal processing complexity in practical systems when no lens (no-lens) is employed;
- We propose an ad-hoc multi-user scheme and we evaluate the related impact of the interference by determining the capability of the proposed architectures to spatially discriminate multiple transmitters while localizing them.

The remainder of the paper is organized as follows. Sec. II contains insights on how to gather position information from the signal wavefront, and Sec. III shows positioning techniques. Sec. IV reports considerations on the interference, and Sec. V describes the achieved results. Conclusions are finally drawn in Sec. VI.

## II. POSITION INFORMATION IN THE SPHERICAL WAVEFRONT

### *A. Operating Frequency Impact*

Before introducing the considered architectures, we investigate the trade-off between the size of the array and the operating frequency to determine the region where the impact of the wavefront curvature is appreciable and hence exploitable for positioning. As usually done, we here consider as a delimiter the Fraunhofer distance  $d_F = 2 D^2/\lambda$ , with  $\lambda$  indicating the wavelength, and  $D$  the antenna diameter. By assuming antennas spaced apart of  $\lambda/2$ , we have  $N_A = 2 D/\lambda$ .

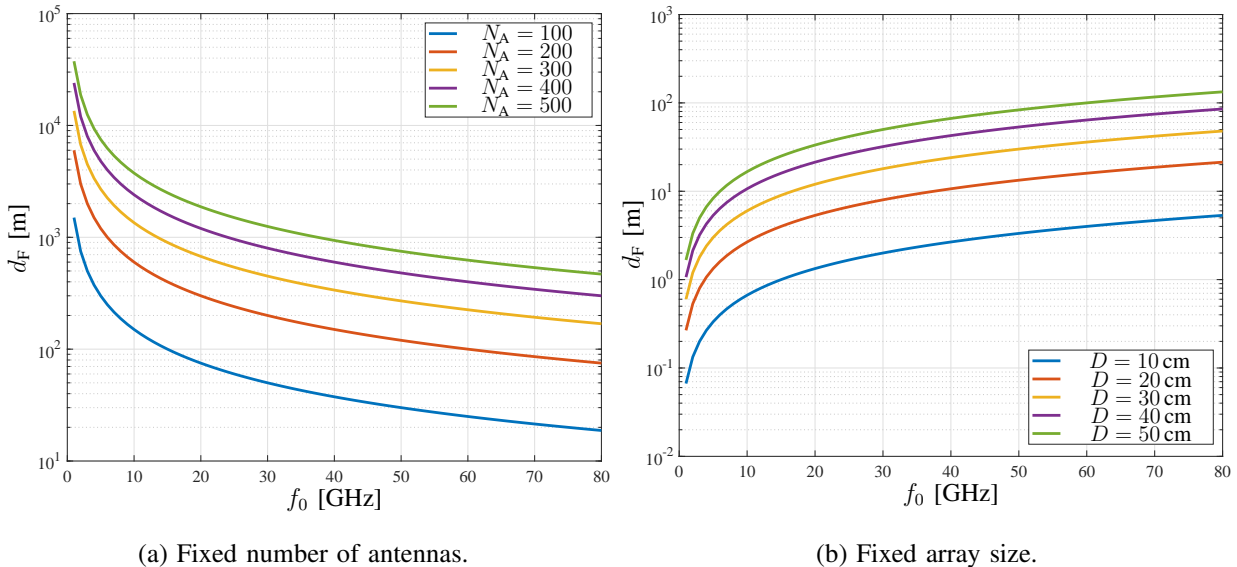


Fig. 2: Starting point of the Fraunhofer region for different frequencies and different array sizes.

The impact of the operating frequency is reported in Fig. 2 for two scenarios. In the first one, the number of employed antennas is kept constant regardless the frequency or the array size. In the latter, the constraint is on the array dimension, as it happens in practical set up where antenna's size limitations are often present. If the constraint is on  $N_A$  (i.e., on RF chains), the curvature effect is more appreciable at lower frequencies as reported in Fig. 2-left. On the other side, if the size of the array is constrained to a certain value, a higher frequency allows to gather a better information on the spherical wavefront (see Fig. 2-right). As an example, for  $D = 50$  cm, the Fraunhofer region, for which the wavefront is considered planar, starts at  $d \simeq 10$  m for  $f_0 = 5$  GHz, and at  $d \simeq 100$  m for  $f_0 = 60$  GHz. Such considerations confirm that the impact of the wavefront curvature is not negligible when large antenna arrays, operating at high frequency, are employed.

In the following, after describing the considered architectures, we will illustrate how positioning is possible with only a single antenna array.

### B. Architectures

In order to exploit the wavefront curvature for positioning, in this paper we consider three different architectures, reported in Fig. 3, involving a device performing the processing at EM level (e.g. a lens) and one or more antenna elements.

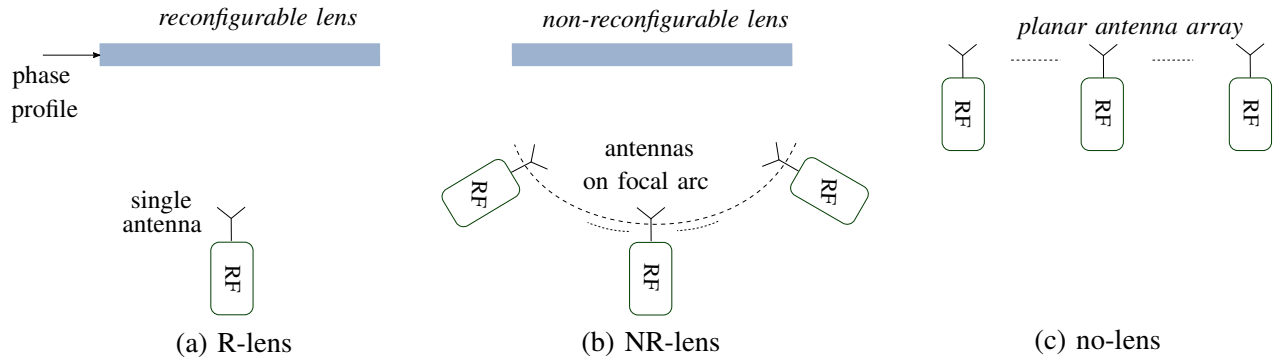


Fig. 3: Lateral view of the considered architectures.

In particular, we aim at investigating the effect on the positioning accuracy when the required processing is split between processing at EM level (e.g., using programmable lens/metasurfaces) and processing at signal level (i.e., processing the RF signal after an antenna element). A different balance between EM level and signal level processing (i.e., a different architecture) translates into a different balance in complexity. To one extreme, where no processing is done at EM level, such as in classical antenna arrays, a large number of antenna elements and RF chains (e.g., LNA, ADC, ..) is required and the complexity is completely put on the processing at RF level. To the other extreme, a R-lens is used and only one antenna/RF chain is required. In this case the complexity is mainly moved to the EM part of the system, i.e., the reconfigurable lens. Between these two extremes, we have chosen a NR-lens that represents a compromise in terms of number of RF chains ( $N_A$  is lower with respect to the no-lens case) and lens fabrication (once the phase profile has been initially realized, it cannot be reconfigured).

In the following, we introduce an ad-hoc general model to retrieve the position information from the incident spherical wavefront.

### C. Signal Model

As previously stated, the EM lens can be realized with different techniques (e.g., metamaterials), and it allows to retrieve the position from an omnidirectional source by exploiting the wavefront curvature.

To this purpose, consider a source transmitting a signal at  $f_0$  and located at position  $\mathbf{p}$ , which is at distance  $d$  from the reference point of the RX located in  $(0, 0, 0)$  (as shown in Fig. 1-right), and denote with  $\Theta = (\theta, \phi)$  the incident angle.

Suppose there are  $N_A$  receiving antennas in positions  $\{\mathbf{p}_n\}$ ,  $n = 0, 1, \dots, N_A - 1$ . Define the surface of the EM lens (if any) lying on the  $YZ$ -plane as  $\mathcal{S}$ , with  $z \in [0, D_z]$ ,  $y \in [0, D_y]$  and  $A_f = D_y D_z$ . Then, we denote with  $\mathbf{r} = [r_0, \dots, r_n, \dots, r_{N_A-1}]^T$  the vector containing the equivalent complex baseband signal received at each antenna, defined as

$$\mathbf{r} = \mathbf{s} + \mathbf{w} = \mathcal{F}_s(h(\mathcal{S}, \mathbf{p})) + \mathbf{w}, \quad (1)$$

where  $\mathbf{w} = [w_0, \dots, w_n, \dots, w_{N_A-1}]^T$  is the vector containing the additive white Gaussian noise (AWGN), i.e.,  $w_n \sim \mathcal{CN}(0, \sigma^2)$ , whereas the useful signal carrying positioning information is

$$\mathbf{s} = [s_0, \dots, s_n, \dots, s_{N_A-1}]^T = \left[ \mathcal{F}_{s_0}(h(\mathcal{S}, \mathbf{p})), \dots, \mathcal{F}_{s_n}(h(\mathcal{S}, \mathbf{p})), \dots, \mathcal{F}_{s_{N_A-1}}(h(\mathcal{S}, \mathbf{p})) \right]^T \quad (2)$$

with  $\mathcal{F}_s(\cdot)$  being the functional representing the operation performed by the EM processing on the signal  $h(y, z, \mathbf{p})$ , observed on each location  $(y, z)$  of the surface due to a source located in  $\mathbf{p}$ , that allows to receive the signal vector  $\mathbf{s}$  at each corresponding antenna. Notably,  $h(y, z, \mathbf{p})$  is given by

$$h(y, z, \mathbf{p}) = A_{\text{pl}} e^{-j\chi} e^{-j2\pi f_0 \tau(y, z, \mathbf{p})} = x_0 e^{-j2\pi f_0 \tau(y, z, \mathbf{p})}, \quad (3)$$

where  $A_{\text{pl}}$  denotes the received signal amplitude,<sup>2</sup> the phase  $\chi \sim \mathcal{U}[0, 2\pi)$  assumes the same value at each antenna and it is uniformly distributed between 0 and  $2\pi$  to model the lack of synchronization between the source and the receiver,  $f_0$  is the central frequency and

$$\tau(y, z, \mathbf{p}) = \frac{\|\mathbf{p} - \mathbf{p}_l(y, z)\| - \|\mathbf{p} - \mathbf{p}_l(0, 0)\|}{c} = \frac{a(y, z, \mathbf{p})}{c}, \quad (4)$$

where  $\mathbf{p}_l(y, z)$  and  $\mathbf{p}_l(0, 0)$  are the generic and the reference points on the EM processing section, respectively, and  $c$  is the speed of light. Thus, the phase profile experienced by the array is composed of an unknown offset  $\chi$  which is common to all the elements of the antenna plus a element-dependent phase shift which depends on the position of the source. Therefore, a suitable processing of the phase profile is sufficient to infer the position of the source provided that also the offset  $\chi$  is estimated, even if it does not carry any information.

According to the reference system of Fig. 1-right, the term  $a(y, z, \mathbf{p})$  is the extra-distance travelled by the wave, which is given by

$$a(y, z, \mathbf{p}) = -d + d \sqrt{1 + \frac{d_{0yz}^2}{d^2} - 2 \cdot \frac{d_{0yz}}{d} g(\Theta, \Theta_{0yz})}, \quad (5)$$

<sup>2</sup>Due to the considered environment geometry, where the receiver antenna is much smaller than the distance, the received signal amplitude assumes approximately the same value at each antenna.



where  $d_{0yz} = \sqrt{y^2 + z^2}$  is the distance of the point with coordinates  $(0, y, z)$  in the surface from its reference point located in  $(0, 0)$ . The term  $g(\Theta, \Theta_{0yz})$  is given by

$$g(\Theta, \Theta_{0yz}) = \sin(\theta) \cos(\phi_{0yz}) , \quad (6)$$

with  $\Theta = (\theta, \phi = 0)$  and  $\Theta_{0yz} = (\theta_{0yz} = \frac{\pi}{2}, \phi_{0yz})$  referring to the target and to the generic point of the aperture with coordinates  $(0, y, z)$ , respectively.<sup>3</sup>

The random phase  $\chi$  includes the complete uncertainty on the received signal phase, since the transmitter and receiver are supposed to be not synchronized and no information can be retrieved from the phase and the TOA of the received signal.

Differently from classical antenna array theory which assumes planar wavefronts (far field condition), here function  $h(y, z, \mathbf{p})$  depends not only on the AOA  $\Theta$  but also on the distance  $d$ , i.e., on the position  $\mathbf{p}$ . Notably, if we consider the signal in the generic  $(0, y, z)$  position of the flat lens performing the EM processing,  $h(y, z, \mathbf{p})$  contains the information on the extra distance traveled by the EM wave to reach the generic coordinate  $(0, y, z)$  of the RX flat lens.

Note that if  $z \ll d$ , according to the second order Taylor-McLaurin series expansion with respect to  $\sqrt{1 + \frac{d_{0yz}^2}{d^2} - 2 \cdot \frac{d_{0yz}}{d} g(\Theta, \Theta_{0yz})}$ , it is

$$a(y, z, \mathbf{p}) \approx -d_{0yz} g(\Theta, \Theta_{0yz}) + \frac{d_{0yz}^2}{2d} (1 - g^2(\Theta, \Theta_{0yz})) , \quad (7)$$

where we have neglected terms including  $1/d^2$  and  $1/d^3$ . In particular, the first term refers to the traditional array phase term containing the AOA information, whereas the second term includes information on the source distance which becomes negligible for large distances.

In the following, we analyze some possible solutions to realize the architectures herein investigated in line-of-sight (LOS) scenario, by discussing their impact on the EM processing or on the array geometry.

1) *EM Processing with a R-lens*: The use of a R-lens that allows to achieve a full control of the phase profile of the signal, represents an extreme case where the complexity is entirely put on the EM processing, and the array is reduced to a single antenna, i.e.,  $N_A = 1$ . Examples of such lenses are reported in [68]. Indeed, despite the technology is not yet mature for the realization of a continuous (e.g., holographic) phase profile, this solution represents a benchmark in complexity entirely put in the lens design.

<sup>3</sup>Note that for a planar aperture lying on the  $YZ$ -plane, it holds  $\theta_{0yz} = 90^\circ$ .

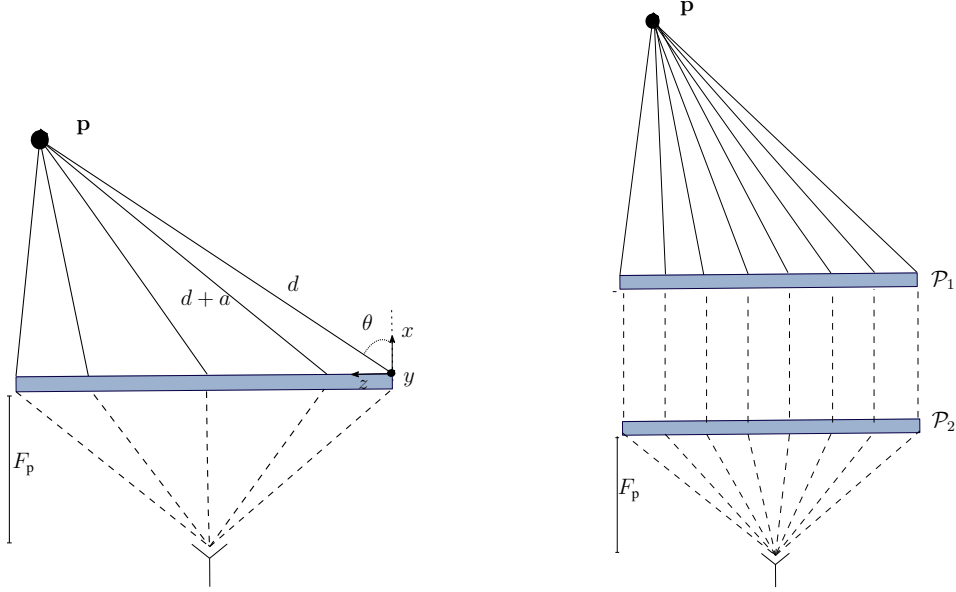


Fig. 4: Left: Lateral-view of the R-lens scenario where the EM processing, realized with a reconfigurable lens, focuses the entire signal towards a single antenna. Right: equivalent processing performed by one R-lens followed by a NR-lens through  $\mathcal{P}_1$  and  $\mathcal{P}_2$ .

In particular, the objective of the R-lens is to focus the impinging wave towards one point, placed in position  $\mathbf{p}_0 = \left[-F_p, \frac{D_y}{2}, \frac{D_z}{2}\right]$  (refer to the coordinates system in Fig. 1-right) at distance  $F_p$  from the lens surface, as shown in Fig. 4. Notably, we can equivalently represent the re-phasing procedure operated by the flat lens by a double-lens system performing two processing operations, namely  $\mathcal{P}_1$  and  $\mathcal{P}_2$ , as depicted in Fig. 4-right. More specifically, through  $\mathcal{P}_1$ , the first lens converts a spherical wavefront into a planar one, with normal direction at its output. On the other side, through the operation  $\mathcal{P}_2$ , the second lens focuses the normal planar incident wavefront into one point, where an antenna is located. Thus,  $\mathcal{P}_2$  does not depend on the source position  $\mathbf{p}$ , i.e., the second lens is a NR-lens, whereas  $\mathcal{P}_1$  concerns the reconfigurable processing that varies with the source position.

According to such considerations on the processing operated by the R-lens, the reconfigurable lens phase profile can be described by a function  $\kappa(y, z, \chi_t, \mathbf{p}_t)$ ,<sup>4</sup> depending on the assumed target position  $\mathbf{p}_t$  and on the test offset  $\chi_t$ , as

$$\kappa(y, z, \chi_t, \mathbf{p}_t) = \mathcal{P}_1(y, z, \chi_t, \mathbf{p}_t) \cdot \mathcal{P}_2(y, z). \quad (8)$$

<sup>4</sup>Differently from  $h(y, z, \mathbf{p})$ , in  $\kappa(y, z, \chi_t, \mathbf{p}_t)$  we make explicit also the dependence on  $\chi_t$ .

In the following, we illustrate the conditions to properly design the phase profiles of the two lenses, that is  $\mathcal{P}_1$  and  $\mathcal{P}_2$ . Note that the distance of the two lenses can be considered negligible.

a) *Design of  $\mathcal{P}_1$* : At the output of the first lens, it is required to obtain a planar wavefront, i.e., the phase of the output EM wave is independent of  $y$  and  $z$ . Due to this consideration,  $\mathcal{P}_1(y, z, \chi_t, \mathbf{p}_t)$  is chosen so that, when the actual source position is in  $\mathbf{p}$  with offset  $\chi$ , it is,

$$\mathcal{P}_1(y, z, \chi_t, \mathbf{p}_t) \cdot h(y, z, \mathbf{p}) = e^{-j\Psi_{0_1}}, \quad (9)$$

where  $\Psi_{0_1}$  is a constant term, so that ideally it should be

$$\mathcal{P}_1(y, z, \chi_t, \mathbf{p}_t) = e^{j(2\pi f_0 \tau(y, z, \mathbf{p}) - \Psi_{0_1})}. \quad (10)$$

b) *Design of  $\mathcal{P}_2$* : Assuming now that the wavefront is planar,  $\mathcal{P}_2(y, z)$  is designed so that the following condition holds

$$\mathcal{P}_2(y, z) \cdot e^{-j\Psi_0(y, z)} = e^{-j\Psi_{0_2}}, \quad (11)$$

where  $\Psi_{0_2}$  is a constant (irrelevant) term and  $\Psi_0(y, z)$  accounts for the travelled distance from a generic point in  $(0, y, z)$  on the second NR-lens surface to the focal point  $F_p$ , that is

$$\Psi_0(y, z) = \frac{2\pi}{\lambda} \sqrt{F_p^2 + \left(y - \frac{D_y}{2}\right)^2 + \left(z - \frac{D_z}{2}\right)^2}. \quad (12)$$

Thus,  $\mathcal{P}_2$  indicates the dephasing term introduced by the NR-lens such that all rays with normal incidence arrive at  $F_p$  with identical phase for constructive superposition. It follows that

$$\mathcal{P}_2(y, z) = e^{j\left(\frac{2\pi}{\lambda} \sqrt{F_p^2 + d_{yz}^2} - \Psi_{0_2}\right)}, \quad (13)$$

where  $d_{yz}^2 = (y - D_y/2)^2 + (z - D_z/2)^2$ . Without loss of generality, in the rest of the manuscript we will assume  $\Psi_{0_1} = \Psi_{0_2} = 0$ . Thus, the signal received at the antenna, after the EM processing operated by the R-lens response (e.g., by the double-lens scheme), can be expressed as

$$r = r_0 = s_0 + w_0, \quad (14)$$

with

$$s_0 = \mathcal{F}_{s_0}(h(\mathcal{S}, \mathbf{p})) = \frac{1}{\lambda \sqrt{D_y D_z}} \int_{D_z} \int_{D_y} \kappa(y, z, \chi_t, \mathbf{p}_t) \cdot h(y, z, \mathbf{p}) e^{-j\Psi_0(y, z)} dy dz. \quad (15)$$

In case  $\mathbf{p}_t = \mathbf{p}$  and  $\chi_t = \chi$ , it holds  $\kappa(y, z, \chi, \mathbf{p}) \cdot h(y, z, \mathbf{p}) e^{-j\Psi_0(y, z)} = 1$ , and the signal received at the antenna simply reduces to

$$r_0 = \sqrt{A_e} \cdot x_0 + w_0, \quad (16)$$

where  $A_e = \frac{D_y D_z}{\lambda^2}$  represents the normalized aperture of the R-lens.

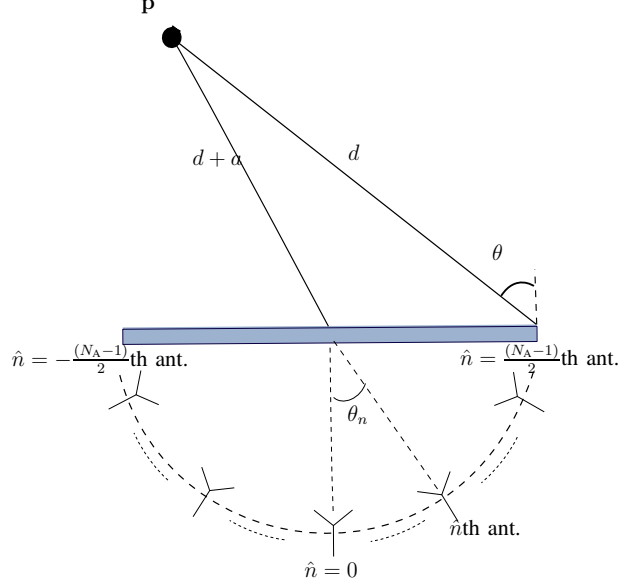


Fig. 5: Top-view of the EM processing, realized with a NR-lens. The use of the lens allows to preserve the number of employed antennas affordable [49].

2) *EM processing with a NR-lens*: We now consider the scenario where the EM processing is realized by means of a NR-lens, placed along the  $yz$ -plane, with size  $D_y \times D_z$ , and a linear antenna array is employed to collect the processed signal, as shown in Fig. 5.<sup>5</sup> In particular, the lens is introduced to collimate the impinging wave in specific directions in analog domain, without the need of complex ad-hoc digital signal processing or metamaterials.

According to the guidelines given in [46], the array is equipped with  $N_A$  antennas located on the focal arc of the lens in  $\{\mathbf{p}_n\} = \left\{ \left( -F_p \cos \theta_n, \frac{D_y}{2}, \frac{D_z}{2} + F_p \sin \theta_n \right) \right\}$ , with  $\theta_n \in [-\pi/2, \pi/2]$ . Then, we consider  $N_A = 1 + \lfloor 2 \tilde{D}_z \rfloor$ , where  $\tilde{D}_z = D_z/\lambda$ , and with  $\lfloor \cdot \rfloor$  denoting the largest integer no greater than its argument [46]. By accounting for a source located on the  $xz$ -plane, the signal received on the focal arc, in the position  $\mathbf{p}_n$ , can be expressed as

$$\begin{aligned} r_n = r(\mathbf{p}_n) &= \mathcal{F}_{s_n}(h(\mathcal{S}, \mathbf{p})) + w_n = s_n(\mathbf{p}) + w_n \\ &= \frac{1}{\lambda \sqrt{D_y D_z}} \int_0^{D_y} \int_0^{D_z} h(y, z, \mathbf{p}) e^{j\Psi_n(y,z)} dz dy + w_n, \end{aligned} \quad (17)$$

<sup>5</sup>We intentionally consider a 2D model in order not to complicate too much the notation. Nevertheless, the extension to a 3D model is straightforward, as done in [47], [69].

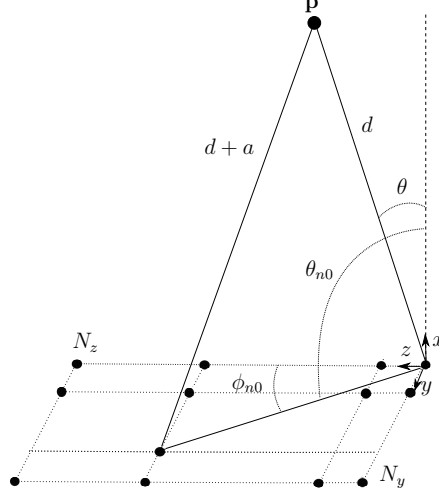


Fig. 6: Scenario for the no-lens, that is, in absence of EM processing.

where

$$\Psi_n(y, z) = \Phi_0 - k_0 \left( z - \frac{D_z}{2} \right) \sin \theta_n, \quad (18)$$

is the dephasing term given by the lens towards the antenna in  $\mathbf{p}_n$ , according to the analysis reported in [46] for an incident planar wavefront, and the normalization term  $1/(\lambda \sqrt{D_y D_z})$  is chosen to guarantee that the overall power intercepted by the lens is proportional to its normalized aperture  $A_e = (D_y D_z)/\lambda^2$  [46]. Moreover,  $\Phi_0$  represents a phase term constant at each antenna. In the following, we assume  $\Phi_0 = 2\pi b$ , with  $b$  any integer. Then, we can write

$$r_n = s_n(\mathbf{p}) + w_n = \frac{x_0}{\lambda \sqrt{D_y D_z}} \int_0^{D_y} \int_0^{D_z} e^{-j2\pi a(y, z, \mathbf{p})} e^{j2\pi \tilde{z} \sin \theta_n} dy dz + w_n, \quad (19)$$

where  $\tilde{z} = \frac{D_z}{2} - z$ , the expression of  $a(y, z, \mathbf{p})$  is given by (5), and  $s_n(\mathbf{p})$  can be expressed by

$$s_n(\mathbf{p}) = \frac{x_0}{\lambda \sqrt{D_y D_z}} \int_0^{D_y} \int_0^{D_z} e^{-j2\pi a(y, z, \mathbf{p})} e^{j2\pi \tilde{z} \sin \theta_n} dy dz. \quad (20)$$

Solving (19) allows to study the impact of the wavefront curvature at the receiver's antennas. Note that in case the wavefront is planar, the solution of (19) reduces the one given in [46].

3) *Post-processing with no-lens*: For comparison purposes, assume now that the EM processing is avoided (baseline scenario), which corresponds to the extreme case with respect to R-lens where all the complexity is entirely put into the receiving array with  $N_A = N_z \times N_y$  antennas placed at an inter-distance of  $\lambda/2$ . We consider such antennas positioned in  $\mathbf{p}_n = (0, n_y \lambda/2, n_z \lambda/2)$  on the receiving surface, with  $n_y = \lfloor \frac{n}{N_z} \rfloor$  and  $n_z = (n \bmod N_z)$ , for

$n = 0, \dots, N_A - 1$ , and it holds  $\mathcal{F}_{s_n}(h(\mathcal{S}, \mathbf{p})) = h(\mathbf{p}_n, \mathbf{p})$ . The RX signal at the  $n$ th antenna element  $r_n$  is simply given by [46]

$$r_n = r(\mathbf{p}_n) = s_n(\mathbf{p}) + w_n = h_n + w_n = x_0 e^{-j2\pi f_0 \tau(\mathbf{p}_n, \mathbf{p})} + w_n. \quad (21)$$

where

$$s_n(\mathbf{p}) = x_0 e^{-j2\pi f_0 \tau(\mathbf{p}_n, \mathbf{p})}. \quad (22)$$

Again, here the information on  $\mathbf{p}$  is embedded in the received signal and, by properly designing the receiver, it is possible to directly infer the position of the transmitter avoiding a prior synchronization phase to align the source and receiving array clocks.

In the following, we derive possible approaches to directly estimate the source location while using the architectures here introduced.

### III. POSITION ESTIMATION

As previously stated, the source positioning task can be achieved by exploiting the curvature of the wavefront, by overcoming the need to tightly synchronize the transmitter and the receiver, which is often unfeasible due to the required interactions for estimating the TOA.

In the following, we describe the adopted positioning approach according to each architecture, in the presence of one source in LOS.

*1) Positioning with R-lens:* In case a R-lens is adopted, for each test position  $\mathbf{p}_t$ , the lens has to be reconfigured. This problem is similar to that of beamforming for phased arrays as in [25], where the signal is available only after the recombination procedure, and one possibility is to pick the configuration that maximizes the output energy. Thus, we can define

$$\ell(\mathbf{p}_t) = |r_0(\mathbf{p}_t)|^2, \quad (23)$$

where  $r_0(\mathbf{p}_t)$  is given by (15) and (14), and the position can be estimated as

$$\hat{\mathbf{p}} = \operatorname{argmax}_{\mathbf{p}_t} \ell(\mathbf{p}_t). \quad (24)$$

Notably,  $\mathbf{p}_t$  is varied within a set of test positions  $\mathcal{P}$  and, consequently, for each  $\mathbf{p}_t$ , a different  $r_0$  is obtained. According to the aforementioned operations, thanks to the processing operated at EM level, the position of the source can be retrieved by using only one antenna and with simple processing operations. Nevertheless, this requires that, for each  $\mathbf{p}_t$ , a different received signal is collected as the lens needs to be reconfigured.

2) *Positioning with NR-lens*: In case a NR-lens is employed, we consider the maximum likelihood (ML) estimator. In our scenario, the likelihood function (depending on the spherical wavefront) is taken with respect to the position  $\mathbf{p}$  of the transmitter and the unknown phase  $\chi$  and it is given by

$$\Lambda(\mathbf{p}, \chi) = p(\mathbf{r}|\mathbf{p}) \propto \prod_{n=1}^{N_A} \exp \left\{ -\frac{1}{2\sigma^2} \left\| r_n - s_n(\mathbf{p}, \chi) \right\|^2 \right\}, \quad (25)$$

with  $\sigma^2 = \mathbb{E}[w_n^2]$ , and where we have made explicit the dependence of  $s_n(\mathbf{p}, \chi)$  on the position  $\mathbf{p}$  and on the phase offset  $\chi$ . Taking the logarithm and discarding all the terms that do not bring contribution for maximizing  $\mathbf{p}$ , the log-likelihood function reduces to

$$\ell(\mathbf{p}, \chi) = \sum_{n=1}^{N_A} \left\{ \Re \left\{ r_n \cdot s_n^*(\mathbf{p}, \chi) \right\} - \frac{1}{2} E_{\text{rx}}(\mathbf{p}) \right\}, \quad (26)$$

where  $E_{\text{rx}}(\mathbf{p}) = \sum_{n=1}^{N_A} E_n(\mathbf{p})$ , with  $E_n(\mathbf{p}) = |s_n(\mathbf{p})|^2$  being the received energy per antenna.

Finally, the ML estimate of the distance can be expressed as

$$\hat{\mathbf{p}} = \arg \max_{\mathbf{p}, \chi} \ell(\mathbf{p}, \chi), \quad (27)$$

that, in accordance with the previous derivation, yields to

$$\hat{\mathbf{p}} = \arg \max_{\mathbf{p}, \chi} \left\{ \sum_{n=1}^{N_A} \Re \left\{ r_n \cdot s_n^*(\mathbf{p}, \chi) \right\} - \frac{1}{2} E_{\text{rx}}(\mathbf{p}) \right\}. \quad (28)$$

According to the analysis in Sec. II, for (28) we have that  $s_n(\mathbf{p}, \chi)$  and  $r_n$  are given by (20) and (19), respectively.

3) *Positioning with no-lens*: For the no-lens case, it is possible to adopt the ML as before in (28) for retrieving the source position, by using (22) and (21) for  $s_n(\mathbf{p}, \chi)$  and  $r_n$ , respectively. Notably, since the EM processing is absent in this case, the number of employed antennas  $N_A$  is higher with respect to the previous case.

The maximization in (28) could involve a certain level of complexity if  $N_A$  is large, therefore in the following we propose a positioning approach entailing a lower complexity for practical systems, and that can be applied only to the no-lens scenario.

a) *Differential Approach*: Consider a uniform planar array where, by adopting the Taylor-McLaurin series expansion in (7),  $h_n$  reported in (21) can be written as

$$\begin{aligned} h_n &\approx x_0 \exp \left\{ -j \frac{2\pi}{\lambda} \left[ \frac{d_{n0}^2}{2d} \left( 1 - g^2(\theta, \phi_{n0}) \right) - d_{n0} g(\theta, \phi_{n0}) \right] \right\} \\ &\approx x_0 \exp \left\{ -j 2\pi \frac{[n_y^2 + n_z^2 \cos^2(\theta)] \lambda}{8d} \right\} \exp \{ j\pi n_z \sin \theta \}, \end{aligned} \quad (29)$$

with  $d_{n0} = \sqrt{(n_y \lambda/2)^2 + (n_z \lambda/2)^2}$  according to Sec. II-C3, and  $\phi_{n0}$  is graphically reported in Fig. 6. Then, for  $n \geq 1$ , we can write

$$h_n h_{n-1}^* = |x_0|^2 \exp \left\{ -j\pi \frac{[(n_y^2 - m_y^2) + (n_z^2 - m_z^2) \cos^2(\theta)] \lambda}{4d} \right\} \exp \{j\pi (n_z - m_z) \sin \theta\}, \quad (30)$$

with  $|x_0|^2 = A_{p1}^2$  and  $m_y = \lfloor \frac{n-1}{N_z} \rfloor$  and  $m_z = ((n-1) \bmod N_z)$ . Thus, the offset term has been removed, and it holds

$$r_n^d = r_n r_{n-1}^* = h_n h_{n-1}^* + w_n^d = s_n^d + w_n^d, \quad n = 2, \dots, N_A, \quad (31)$$

with  $s_n^d = h_n h_{n-1}^*$ , and  $w_n^d = w_n w_{n-1}^* + w_n h_{n-1}^* + w_{n-1}^* h_n$  contains the noise terms at the output of the differential operation. The position can now be estimated as follows

$$\hat{\mathbf{p}} = \arg \max_{\mathbf{p}} \left\{ \sum_{n=2}^{N_A} \left( r_n^d \cdot [s_n^d]^* \right) - \frac{1}{2} E_{\text{rx}}^d(\mathbf{p}) \right\}, \quad (32)$$

where  $E_{\text{rx}}^d = \sum_{n=2}^{N_A} |s_n^d|^2$ . In a worst-case in terms of complexity, when an exhaustive search is used, the ML only compares a number of test positions and selects the maximum as an estimate of the position, without searching over all possible phase offset  $\chi$ , thanks to the use of the proposed differential scheme.

In fact, the approach in (28) entails the construction of a 3D matrix with size  $(N_{\text{array}} \times N_{\mathbf{p}_t} \times N_{\chi_t})$  where  $N_{\mathbf{p}_t}$  and  $N_{\chi_t}$  are the number of tests for position and offset, respectively. Contrarily, with the proposed approach, the search in (32) reduces to a matrix with size  $(N_{\text{array}} \times N_{\mathbf{p}_t})$ .

In the numerical results the performance of the described approaches will be evaluated.

#### IV. MULTI-SOURCE INTERFERENCE

The intent of the previous section was to establish how the position of a source can be determined with the proposed signal model. On the other side, real environments are usually characterized by the presence of multiple simultaneously transmitting sources. To this purpose, we investigate here the impact of the interference when discriminating an intended useful source from one or more interference transmitters. Indeed, the established performance is related to the positioning resolution of the system.

Let us now assume that interference sources, in addition to the intended useful one, are simultaneously transmitting in the same environment. In this case, the received signal is

$$\mathbf{r} = \mathbf{s}_u + \mathbf{s}_{\text{int}} + \mathbf{w} = \mathcal{F}_s(h(\mathcal{S}, \mathbf{p}_u)) + \sum_{i=1}^{N_{\text{int}}} \mathcal{F}_s(h(\mathcal{S}, \mathbf{p}_i)) + \mathbf{w}, \quad (33)$$



where  $s_u$  and  $s_{\text{int}}$  refer to the contribution from the intended useful source, located in  $\mathbf{p}_u$  with phase offset  $\chi_u$ , and from the interfering  $i$ th source, located in  $\mathbf{p}_i$  and with phase offset  $\chi_i$ , respectively. The signal received at the  $n$ th antenna is

$$r_n = s_{u,n} + \sum_{i=1}^{N_{\text{int}}} s_{i,n} + w_n. \quad (34)$$

In the following, in order to evaluate the impact of the interference, we first consider an ideal scenario where the position of the intended useful source is assumed to be perfectly estimated (e.g., according to the approach of Sec. III). Notably, this corresponds to a phase profile matched to the received phase profile, that is  $\hat{\mathbf{p}} = \mathbf{p}_u$  and  $\chi = \chi_u$ , which corresponds to a maximal-ratio combining (MRC). Successively, we evaluate the signal-to-interference ratio (SIR) in order to determine the performance degradation due to the interference. The output of the MRC can be expressed as

$$\ell_{\text{MRC}}(\mathbf{p}_u, \chi_u) = \eta_u + \eta_{\text{int}} + \eta_w, \quad (35)$$

where  $\eta_u$ ,  $\eta_{\text{int}}$  and  $\eta_w$  correspond to the processed versions of the useful, interference and noise contribution, respectively, and they are defined in the following for each architecture. Nevertheless, according to the considered model, we define the SIR as

$$\text{SIR} = \frac{|\eta_u|}{|\eta_{\text{int}}|}. \quad (36)$$

In the following, considerations are drawn for each architecture.

#### A. SIR using R-lens

Due to the aforementioned considerations, in case of a R-lens, for the MRC we have  $\kappa(y, z, \chi_t, \mathbf{p}_t) = \kappa(y, z, \chi_u, \mathbf{p}_u)$ . Thus, for this case it holds  $\eta_u = w$  and, assuming that the phase-profile of the R-lens is perfectly matched to the received signal phase, according to (14), (15) and (16) we have

$$\eta_u = \frac{A_f}{\lambda \sqrt{D_y D_z}} x_0, \quad (37)$$

with  $A_f = D_y D_z$ , and  $\eta_{\text{int}}$  is given by

$$\eta_{\text{int}} = \frac{x_0}{\lambda \sqrt{D_y D_z}} \cdot \sum_{i=1}^{N_{\text{int}}} \eta_i, \quad (38)$$

where

$$\eta_i = e^{j(\chi_u - \chi_i)} \int_{D_z} \int_{D_y} e^{j2\pi f_0(\tau(y,z,\mathbf{p}_u) - \tau(y,z,\mathbf{p}_i))} dydz. \quad (39)$$

Thus, the SIR for the R-lens can be expressed as

$$\text{SIR}_{\text{R-lens}} = \frac{A_f}{\left| \sum_{i=1}^{N_{\text{int}}} \eta_i \right|}. \quad (40)$$

Then, assume the presence of only one generic interfering user, with  $\chi_i = \chi_u$ , i.e., a worst case scenario. For a given  $\mathbf{p}_u$ , i.e.,  $d$  and  $\theta$ , we can evaluate the impact of the interference according to  $\mathbf{p}_i = (d + \Delta d, \theta + \Delta\theta)$ , where the couple  $(\Delta d, \Delta\theta)$  represents the variation of  $\mathbf{p}_i$  from  $\mathbf{p}_u$  along  $d$  and  $\theta$ . Thus, by expliciting the dependence of  $\eta_{\text{int}}$  on  $\Delta d$  and  $\Delta\theta$ , we can write

$$\eta_i(\Delta d, \Delta\theta) = \int_{D_z} \int_{D_y} e^{j2\pi f_0[\tau(y,z,d,\theta) - \tau(y,z,d+\Delta d,\theta+\Delta\theta)]} dydz. \quad (41)$$

To this purpose, in order to make use of the expression in (4), we consider the approximation reported in (7), in the following way

$$\begin{aligned} a(y, z, \mathbf{p}_u) &\approx -z \sin \theta + \frac{y^2}{2d} + \frac{z^2 \cos^2(\theta)}{2d}, \\ a(y, z, \mathbf{p}_i) &\approx -z \sin(\theta + \Delta\theta) + \frac{y^2}{2(d + \Delta d)} + \frac{z^2 \cos^2(\theta + \Delta\theta)}{2(d + \Delta d)}, \end{aligned} \quad (42)$$

that gives to

$$\begin{aligned} \eta_i(\Delta d, \Delta\theta) &= \\ &\int_{D_z} \int_{D_y} \exp \left\{ j \frac{2\pi}{\lambda} \left( z [\sin(\theta + \Delta\theta) - \sin \theta] + \frac{y^2}{2d} \left( 1 - \frac{1}{1 + \frac{\Delta d}{d}} \right) + \frac{z^2}{2d} \left[ \cos^2 \theta - \frac{\cos^2(\theta + \Delta\theta)}{1 + \frac{\Delta d}{d}} \right] \right) \right\} dydz. \end{aligned} \quad (43)$$

From (43) it is not easy to get insights about the impact of various parameters on the SIR. A possibility to simplify the model is to consider only distance variations  $\Delta d$ , with  $\Delta\theta = 0$ , by assuming  $\cos \theta \approx 1$ , which is true when users are close to the boresight direction. Thus, we can write

$$\eta_i(\Delta d, 0) \approx \int_{D_z} \int_{D_y} \exp \left\{ j \frac{2\pi}{\lambda} \left( \frac{y^2 + z^2}{2d} \left( 1 - \frac{1}{1 + \frac{\Delta d}{d}} \right) \right) \right\} dydz, \quad (44)$$

and, in order to get an approximate closed-form of (43), we change from Cartesian to polar coordinates  $(\rho, \varphi)$ , indicating a point on the surface, and we approximate the surface of the lens with a quadrant of a circle with radius  $D_\rho$ , such that  $\frac{\pi D_\rho^2}{4} = D_z D_y$ , thus obtaining

$$\begin{aligned} \eta_i(\Delta d, 0) &\approx \int_0^{D_\rho} \int_0^{\pi/2} \exp \left\{ -j \frac{2\pi}{\lambda} \left( \frac{\rho^2}{2d} \left( \frac{1}{1 + \frac{\Delta d}{d}} - 1 \right) \right) \right\} \rho d\rho d\varphi \\ &\approx A_f \left[ e^{-j \frac{\pi}{\lambda} D_\rho^2 \gamma} \text{sinc} \left( \frac{D_\rho^2 \gamma}{\lambda} \right) \right], \end{aligned} \quad (45)$$

where

$$\gamma = \frac{1}{2d} \left( \frac{1}{1 + \frac{\Delta d}{d}} - 1 \right). \quad (46)$$

Notably, when  $\Delta d = 0$ , i.e.,  $\gamma = 0$ , it is  $\eta_i(0, 0) = A_f$ . Coming back to (40), we can now determine when the SIR is above a certain threshold  $\xi^*$ , that is,

$$\text{SIR}_{\text{R-lens}} = \frac{\eta_u}{|\eta_i(\Delta d, 0)|} = \frac{1}{\left| \text{sinc} \left( \frac{D_\rho^2}{2\lambda d} \left( \frac{1}{1 + \frac{\Delta d}{d}} - 1 \right) \right) \right|} > \xi^*. \quad (47)$$

Result in (47) is useful to determine the distance interval  $\Delta d$  which is vulnerable to the interference, in other words, the minimum spacing  $\Delta d$  between users such that it holds  $\text{SIR} > \xi^*$ . In particular, when  $d \gg D_\rho$ , i.e.,  $d \gg D_y$ ,  $d \gg D_z$ , the argument of the sinc-function tends to be 0, and consequently the SIR to 1, representing a worst case scenario. Thus, in such conditions the wavefront curvature becomes weak and it becomes difficult to discriminate the position of two transmitters. To better picture these considerations, note that since  $\text{sinc}(x)$  has a  $1/(\pi x)$  envelope, (47) is surely satisfied for

$$\left| \frac{2A_f}{\lambda d} \left( \frac{\Delta d}{d + \Delta d} \right) \right| > \xi^*. \quad (48)$$

Notably, according to (48), the relation of  $d$  with the physical aperture  $A_f$  and with  $\Delta d$  plays an important role in determining the capability to discriminate the useful source from an interference one. Indeed, large values of  $2A_f/(\lambda d)$  allow to relax the requirement on  $\Delta d$  for attaining a SIR above  $\xi^*$ .

### B. SIR using NR-lens

Differently from before, in this case the output of the MRC is given by

$$\eta_u = \sum_{n=1}^{N_A} s_{u,n} \cdot s_n^*(\mathbf{p}_u, \chi_u), \quad \eta_{\text{int}} = \sum_{n=1}^{N_A} \sum_{i=1}^{N_{\text{int}}} s_{i,n} \cdot s_n^*(\mathbf{p}_u, \chi_u), \quad \eta_w = \sum_{n=1}^{N_A} w_n \cdot s_n^*(\mathbf{p}_u, \chi_u), \quad (49)$$

with

$$\begin{aligned} s_{u,n} &= \frac{x_0}{\lambda \sqrt{D_y D_z}} \int_0^{D_y} \int_0^{D_z} e^{-j2\pi a(y,z,\mathbf{p}_u)} e^{j2\pi \tilde{z} \sin \theta_n} dy dz \\ s_{i,n} &= \frac{x_0}{\lambda \sqrt{D_y D_z}} \int_0^{D_y} \int_0^{D_z} e^{-j2\pi a(y,z,\mathbf{p}_i)} e^{j2\pi \tilde{z} \sin \theta_n} dy dz, \end{aligned} \quad (50)$$

and they are characterized by the same lens response, regardless the value of  $\mathbf{p}_u$ , since the lens is designed with a fixed phase profile. Indeed, the source position is inferred according to the focusing of the received signal towards the array placed behind the lens [46]. By means of the above equations, the SIR for multiple interference can be found by using (36).

Then, for the single interference case, by assuming again the approximation of  $(\theta, \Delta\theta) = (0, 0)$ , and by injecting (42) and (50) into (49), the evaluation of  $\eta_u$  and  $\eta_{\text{int}} = \frac{x_0^2}{\lambda^2 A_f} \eta_i(\Delta d, 0)$  now requires the resolution of the following equations

$$\begin{aligned} \eta_u &= \frac{x_0^2}{\lambda^2 A_f} \sum_{n=1}^{N_A} \left| \int_{D_z} \int_{D_y} e^{-j\frac{2\pi}{\lambda} \left[ \frac{y^2+z^2}{2d} - \tilde{z} \sin \theta_n \right]} dy dz \right|^2 \\ \eta_i(\Delta d, 0) &= \sum_{n=1}^{N_A} \left\{ \left[ \int_{D_z} \int_{D_y} e^{-j\frac{2\pi}{\lambda} \left[ \frac{y^2+z^2}{2(d+\Delta d)} - \tilde{z} \sin \theta_n \right]} dy dz \right] \left[ \int_{D_z} \int_{D_y} e^{-j\frac{2\pi}{\lambda} \left[ \frac{y^2+z^2}{2d} - \tilde{z} \sin \theta_n \right]} dy dz \right]^* \right\}, \end{aligned} \quad (51)$$

which give

$$\text{SIR}_{\text{NR-lens}} = \frac{\sum_{n=1}^{N_A} \left| \int_{D_z} \int_{D_y} e^{-j\frac{2\pi}{\lambda} \left[ \frac{y^2+z^2}{2d} - \tilde{z} \sin \theta_n \right]} dy dz \right|^2}{|\eta_i(\Delta d, 0)|} > \xi^*. \quad (52)$$

In this case it is not possible to obtain simple expressions but their numerical solution allows to determine the values of the  $\text{SIR}_{\text{NR-lens}}$  for different values of  $d, \theta, \Delta d$ , as shown in Sec. V.

### C. SIR using no-lens

The same expressions as in (50) hold also for the no-lens scenario. In particular, in this case we have

$$\eta_u = x_0^2 N_A, \quad \eta_{\text{int}} = x_0^2 \sum_{i=1}^{N_{\text{int}}} \eta_i, \quad (53)$$

with

$$\eta_i = e^{j(\chi_u - \chi_i)} \sum_{n=1}^{N_A} e^{j2\pi f_0(\tau(\mathbf{p}_n, \mathbf{p}_u) - \tau(\mathbf{p}_n, \mathbf{p}_i))}, \quad (54)$$

that allows us to write

$$\text{SIR}_{\text{no-lens}} = \frac{N_A}{\left| \sum_{i=1}^{N_{\text{int}}} \eta_i \right|}. \quad (55)$$

By making the approximations  $\eta_{\text{int}} = \eta_i(\Delta d, 0)$  as in Sec. IV-A, we can write (36) as

$$\text{SIR}_{\text{no-lens}} = \frac{N_A}{\left| \sum_{n=1}^{N_A} e^{-j \frac{2\pi}{\lambda} \gamma d_{n0}^2} \right|} > \xi^*, \quad (56)$$

where  $d_{n0}$  is defined below (29),  $n_y$  and  $n_z$  are given in Sec. II-C3, and  $\gamma$  is given by (46).

Notably, since

$$\left| \sum_{n=1}^{N_A} e^{-j \frac{2\pi}{\lambda} \gamma d_{n0}^2} \right| \leq \sum_{n=1}^{N_A} \left| e^{-j \frac{2\pi}{\lambda} \gamma d_{n0}^2} \right| = N_A, \quad (57)$$

we obtain  $\text{SIR}_{\text{no-lens}} \geq 1$ .

Again, the values of  $\Delta d$  satisfying (56) represent the areas where the system is robust with respect to the interference. As an example, if  $\Delta d/d \ll 1$ ,  $\gamma \approx 0$  that yields to  $\text{SIR}_{\text{no-lens}} \approx 0$  dB.

## V. NUMERICAL RESULTS

In this section, the different architectures are compared in terms of positioning performance and interference rejection in some specific configurations. In particular, we first consider a single user scenario and, successively, we move to the multi-user case in order to appreciate the capability to discriminate an intended useful source in presence of interference. In all the configurations we discuss about the complexity trade-off, evidencing the cost in terms of performance loss when the number of RF chains is reduced. In fact, for a fixed aperture  $A_e$ , a different number of antennas (and hence RF processing chains) is required to each architecture, as shown in Table. I. Thus, there are two competing effects. From one side, a higher complexity in the processing at EM level allows to reduce the number of RF chains. In fact, in the extreme scenario of the R-lens, it holds  $N_A = 1$ , regardless the choice of the aperture (see Fig. 7) but a reconfigurable phase profile should be designed for the lens. When no EM processing is adopted, there is the need to employ large  $N_A$  (i.e., a large number of RF chains), as for the no-lens. In between, there is the trade-off offered by the NR-lens, where the number of antennas depends on the geometry, i.e., on the choice of  $D_z$ , but it is required to perform some processing in the analog domain with a NR-lens.

In the following, if not otherwise indicated, we consider rectangular areas with  $D_y = 2.5$  cm in all scenarios, and  $D_z = 10$  cm,  $D_z = 15$  cm and  $D_z = 20$  cm that correspond to normalized areas of  $A_e = D_y D_z / \lambda^2 = 100$ ,  $A_e = 150$  and  $A_e = 200$ , respectively.

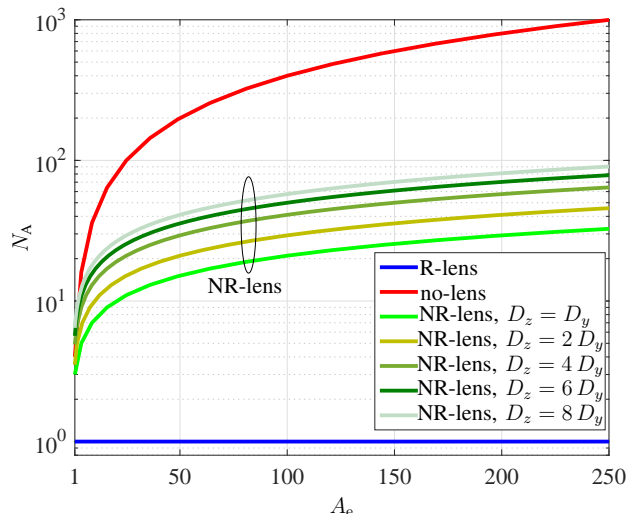


Fig. 7: Number of required antennas for each configuration.

TABLE I: Complexity trade-off as a function of  $A_e$ .

Architecture	Required RF Chains	EM Processing
R-lens	$N_A = 1$	reconfigurable lens
NR-lens	$N_A = 1 + \lfloor 2 \frac{A_e \lambda}{D_y} \rfloor$	non-reconfigurable
no-lens	$N_A = \lfloor 4 A_e \rfloor$	absent

### A. Single-User Scenario

a) *Simulation Scenario*: In accordance with the analysis of Sec. III, we now evaluate the position estimation performance in a single-user scenario. We consider a transmitter sending a signal centered at  $f_0 = 60$  GHz, with an effective radiated isotropic power (EIRP) of 23 dBm. At the receiver, we account for a noise power of  $-106$  dBW, and the parameter  $A_{pl}$  of (3) is obtained from the link budget in free-space condition.

Results are expressed in terms of the root mean square error (RMSE) of the position estimate, which is evaluated as

$$\text{RMSE}(\mathbf{p}) = \sqrt{\frac{1}{N_c} \sum_{m=1}^{N_c} \|\hat{\mathbf{p}}_m - \mathbf{p}\|^2}, \quad (58)$$

where  $N_c$  is the number of Monte Carlo iterations considered in simulations and  $\hat{\mathbf{p}}_m$  is the position estimate at the  $m$ th iteration. In particular, for each iteration, a different noise realization is generated according to  $\sigma^2$ , as well as a different realization of phase  $\chi$ , which is kept the

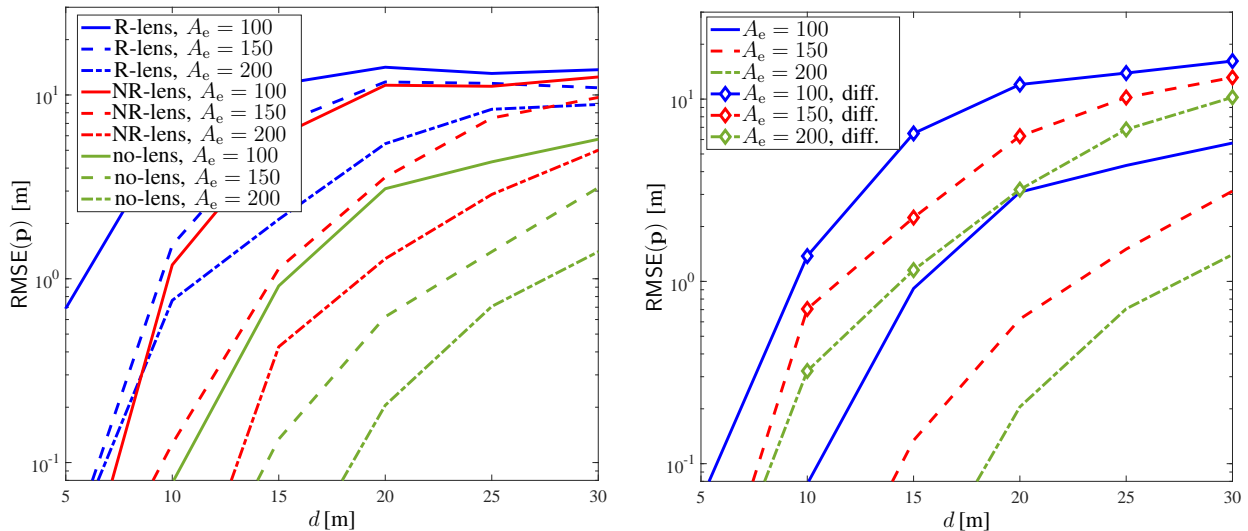


Fig. 8: RMSE as a function of the TX-RX distance  $d$ , fixed AOA =  $0^\circ$  and different architectures (left), and comparison between ML and differential estimation for no-lens (right).

same for all the antennas. In this way, the random phase models a complete clock mismatch between the transmitter and the receiver.

*b) RMSE for Different Source Distance:* Figure 8-left reports the obtained results for the different schemes and  $A_e$ , using the ML position estimator in (28) for the NR-lens and no-lens, and the position estimator in (24) for the R-lens. We initially fixed the AOA to  $0^\circ$  by varying only the TX-RX distance from 5 m to 30 m. As evidenced in the figure, the larger is  $A_e$  the better is the position estimate thanks to the increased physical area that permit to collect a larger amount of power and exploit better the wavefront curvature.

The no-lens-based solution provides the best performance thanks to the employment of  $N_A$  antennas (and RF chains), at the expense of a much higher complexity at RF level. Nevertheless, the use of a R-lens with  $N_A = 1$  (only one RF chain) allows to attain a sub-meter RMSE for  $d = 10$  m. In between, the NR-lens represents the trade-off in terms of RF ( $N_A$ ) and EM processing (lens) complexity. This effect is more pronounced for larger distances, where the path loss increases. In fact, as an example, for NR-lens with  $A_e = 250$  and  $N_A = 81$ , the positioning error is kept below 1 cm at  $d = 10$  m, and at about 1 m for  $d = 20$  m whereas, for the no-lens scenario, the same error of 1 m is made at about  $d = 30$  m. Such a localization performance is obtained for a physical area  $A_f = (10 \times 2.5) \text{ cm}^2$ ,  $A_f = (15 \times 2.5) \text{ cm}^2$  and  $A_f = (20 \times 2.5) \text{ cm}^2$ , which are extremely compact and, thus, suitable for real scenarios, e.g.,

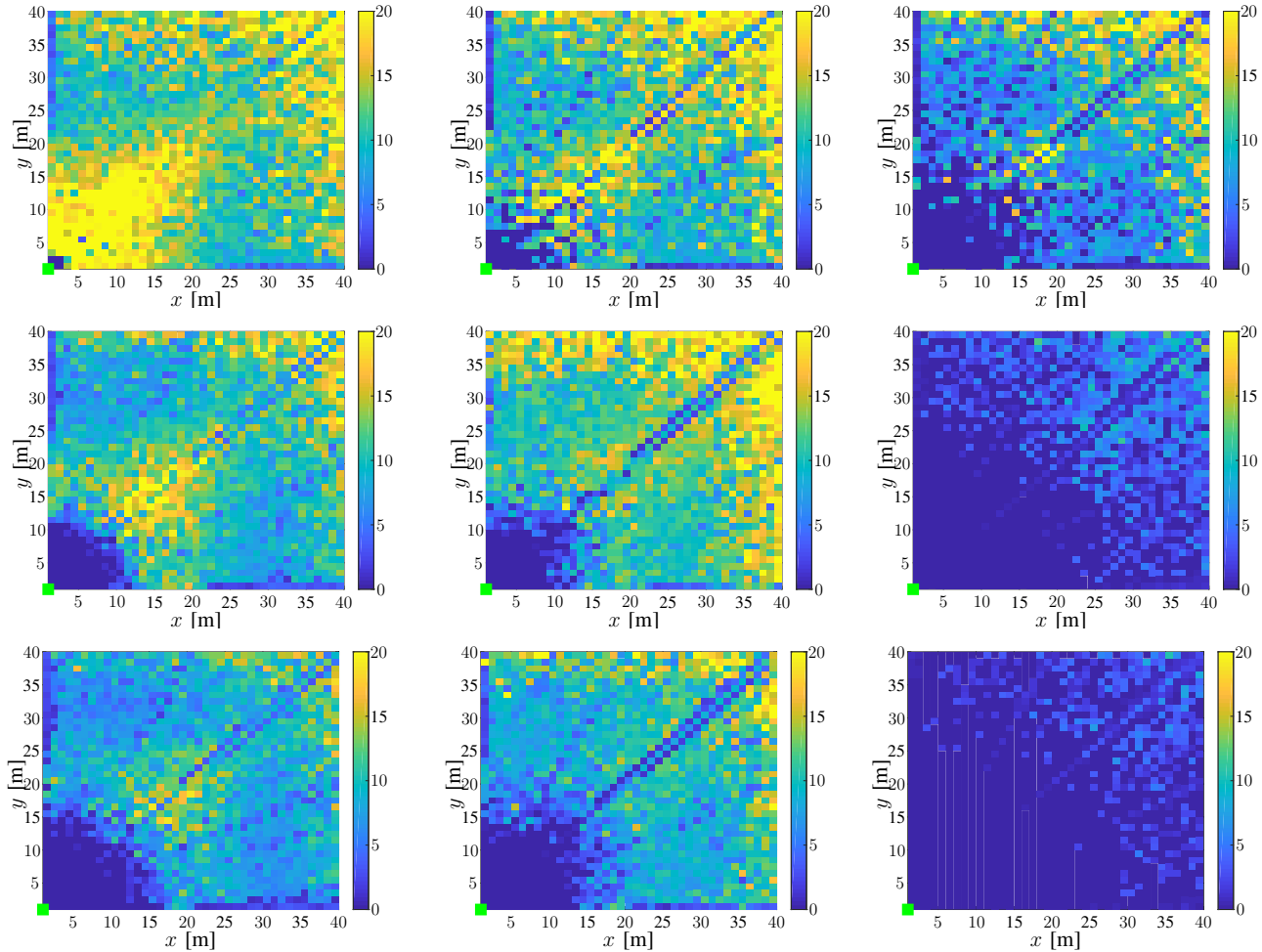


Fig. 9: RMSE maps (errors in meters) for R-lens (left), NR-lens (middle) and no-lens (right), for  $A_e = 100$  (top),  $A_e = 150$  (middle) and  $A_e = 200$  (bottom).

for an integration in future generation of access points. Note also that the receiver noise plays a crucial role as well. In fact, despite when the source is located at the Fraunhofer distance the wavefront can be approximated to be planar, the receiver is still capable to infer the transmitter position if the noise contribution is not extremely large.

In case of no-lens and NR-lens, the performance has been obtained using the ML estimator which, from one hand provides a useful benchmark, but from the other hand it might entail a high signal processing complexity, since it requires the search along the phase offset and the position. In this sense, the differential approach proposed in Sec. III-3a allows to avoid a bi-dimensional search (i.e., over  $\chi$  and  $\mathbf{p}$ ).

Results are reported in Fig. 8-right and they are encouraging, since performance is still reliable



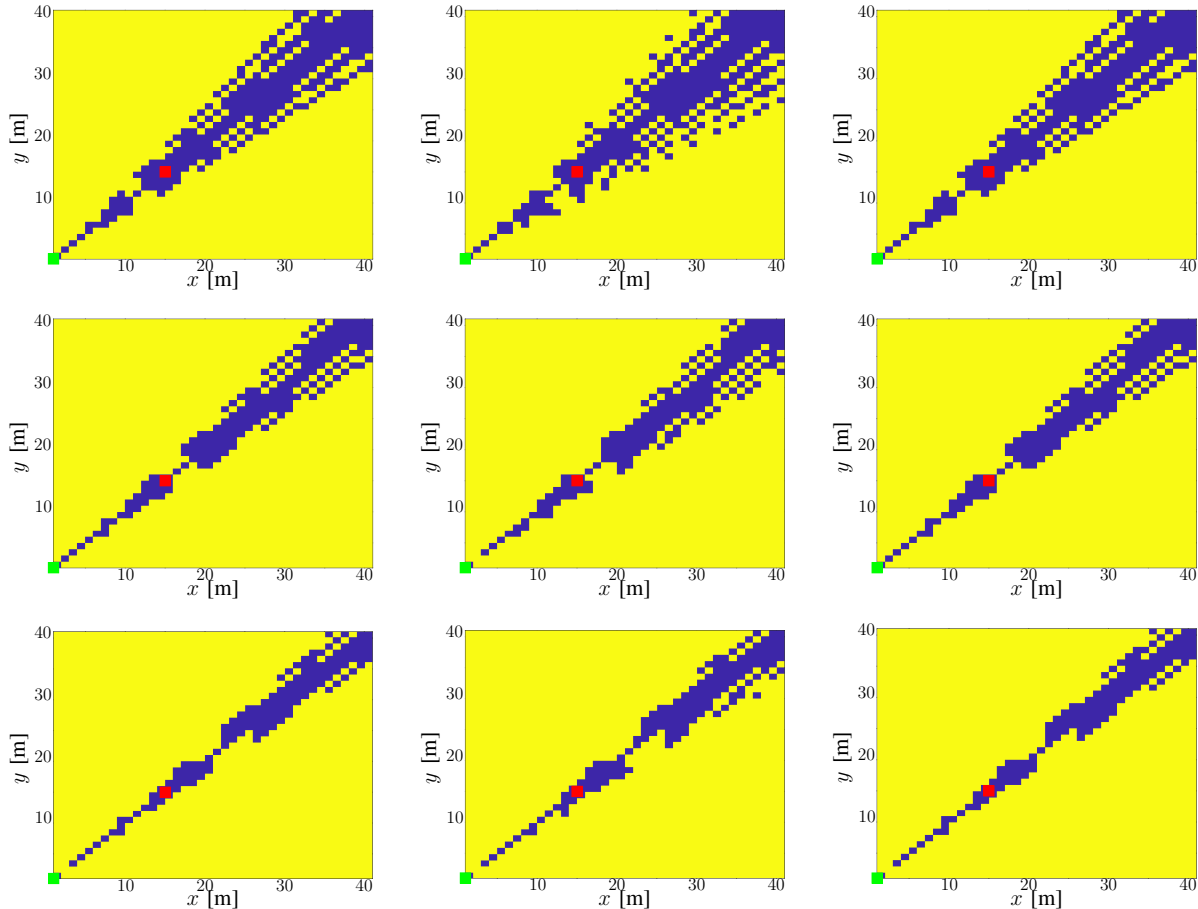


Fig. 10: Coverage for a transmitter placed at  $d \simeq 20$  m and one interference place in different position. Blue and yellow points denote SIR below or above 10 dB, respectively. Left: no-lens. Middle: NR-lens. Right: R-lens. From top to bottom:  $A_e = 100$ ,  $A_e = 150$ ,  $A_e = 200$ .

(i.e.,  $\text{RMSE}(\mathbf{p}) \approx 3$  m at  $d = 20$  m for  $A_e = 200$ ) with the advantage that the computational complexity of the positioning algorithm can be reduced.

*c) RMSE for Different Source Angle and Distance:* Finally, the aforementioned considerations for the different architectures are corroborated by the RMSE maps reported in Fig. 9 for different  $A_e$ . They are obtained by placing the receiver (i.e., the green square marker) in  $(0, 0)$  rotated towards the center of the area, i.e., towards the red marker, and by alternatively placing the transmitting source in all the grid points of the environment. For the considered scenario, in accordance with the results reported in Fig. 8-left, the no-lens provides the best performance thanks to the larger number of antennas involved in the curvature processing.

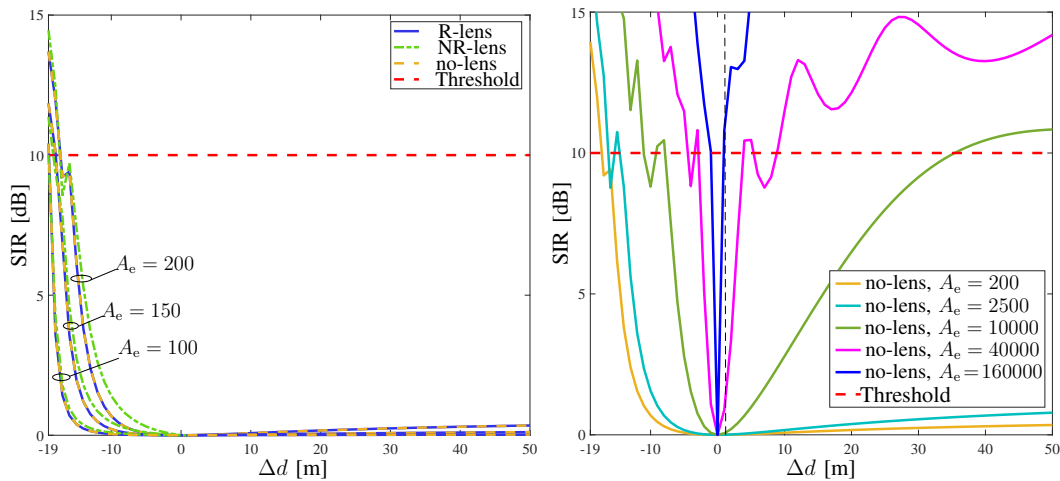


Fig. 11: Interference discrimination for fixed  $\theta = 0^\circ$ , with useful distance  $d = 20$  m, interference distance  $d + \Delta d$ , and different  $A_e$ . Left: different architectures. Right: no-lens case.

## B. Multi-User Scenario

1) *Single Interference Scenario*: We first evaluate the SIR when there is another interference source located in the environment. To that purpose, we considered a square room with size  $(40 \times 40) \text{ m}^2$ , represented with a grid of points with dimension  $(1 \times 1) \text{ m}^2$ . Then, we fixed the RX (green square marker), rotated of  $45^\circ$  oriented towards the center of the room, in  $(0, 0)$  and we located the useful TX (red square marker) in  $(15, 15)$ , while alternatively placing the interference in each point for computing the SIR. In particular, we considered a target SIR threshold  $\xi^* = 10$  dB, which is a typical value in multi-user schemes, and we discriminate yellow points from the blue points if the SIR is above the threshold (coverage). In this sense, results reported in Fig. 10 show the impact of the antenna architecture, when the intended useful source is at a distance of about 20 m (red marker) from the receiver (green marker), and for different  $A_e$ . Notably, the interference effect is such that it is mainly affected by the AOA and it is not possible to discriminate the user if an interference one is on the same direction.

To better investigate this detrimental effect, in Fig. 11-left we evaluated the SIR by using (40), (52) and (55), with the source at  $d = 20$  m with  $\theta = 0^\circ$ , while positioning the interfering user  $\Delta d$  far away from the useful one. More specifically,  $\Delta d = 0$  m indicates that the two users are exactly juxtaposed (i.e.,  $d_i = d$ ), whereas  $\Delta d = -19$  m means that  $d_i \approx 1$  m. Indeed, for the three architectures the SIR is almost always below the threshold when the interfering user is  $\Delta d$  away from the useful one. We ascribe this effect to the fact that when  $d \gg D_z, D_y$ , it is

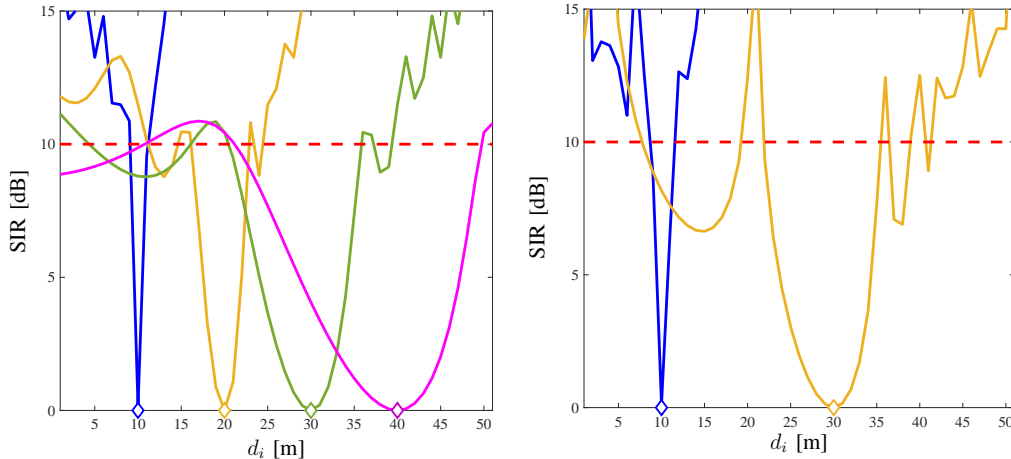


Fig. 12: Interference discrimination for  $A_e = 40,000$ , i.e.,  $A_f = 1 \text{ m}^2$ , when the transmitter is in different positions (diamonds), for no-lens (left) and R-lens (right). Different colors represent the different tested distances.

not possible to discriminate close transmitting sources. This is corroborated also by the results reported in Fig. 11-right obtained by using (56), where the same conditions are preserved, but  $A_e$ , i.e.,  $A_f$ , is increased such that the SIR becomes larger than the threshold.

To further investigate the problem, in Fig. 12-left and Fig. 12-right we considered the approximated expressions in (56) (no-lens) and in (47) (R-lens), respectively, for  $A_f = 1 \text{ m}^2$  ( $A_e = 40,000$ ). In particular, we accounted for different values of the useful source distances (diamond markers), while the distance of one interfering source is varied. As an example, the point of the green curve in  $d_i = 20 \text{ m}$  represents the SIR value when the useful source is at  $d = 30 \text{ m}$ , and  $\Delta d = 10 \text{ m}$ . According to Fig. 12-left, if  $d_i = 10 \text{ m}$  and  $d + \Delta d > 11 \text{ m}$  or  $d - \Delta d < 9 \text{ m}$ , for the no-lens the receiver is capable to discriminate the two users only through the position with high precision, since a SIR larger than 10 dB is guaranteed. The same considerations are valid for the NR-lens in Fig. 12-right. When instead  $d = 30 \text{ m}$ , in both figures a larger  $\Delta d$  does not automatically imply robustness against the interference. In fact, for  $d + \Delta d = 15 \text{ m}$ , it holds  $\text{SIR} < 10 \text{ dB}$ .

2) *Multi-Interference Scenario*: Now we consider a scenario with multiple interferers, and the intended useful source alternatively placed in each grid point of the environment. Notably, for each TX position and for each Monte Carlo iteration, interference is generated and distributed in the considered environment according to a Poisson point process (PPP) with intensity  $\lambda_p = 5$ .

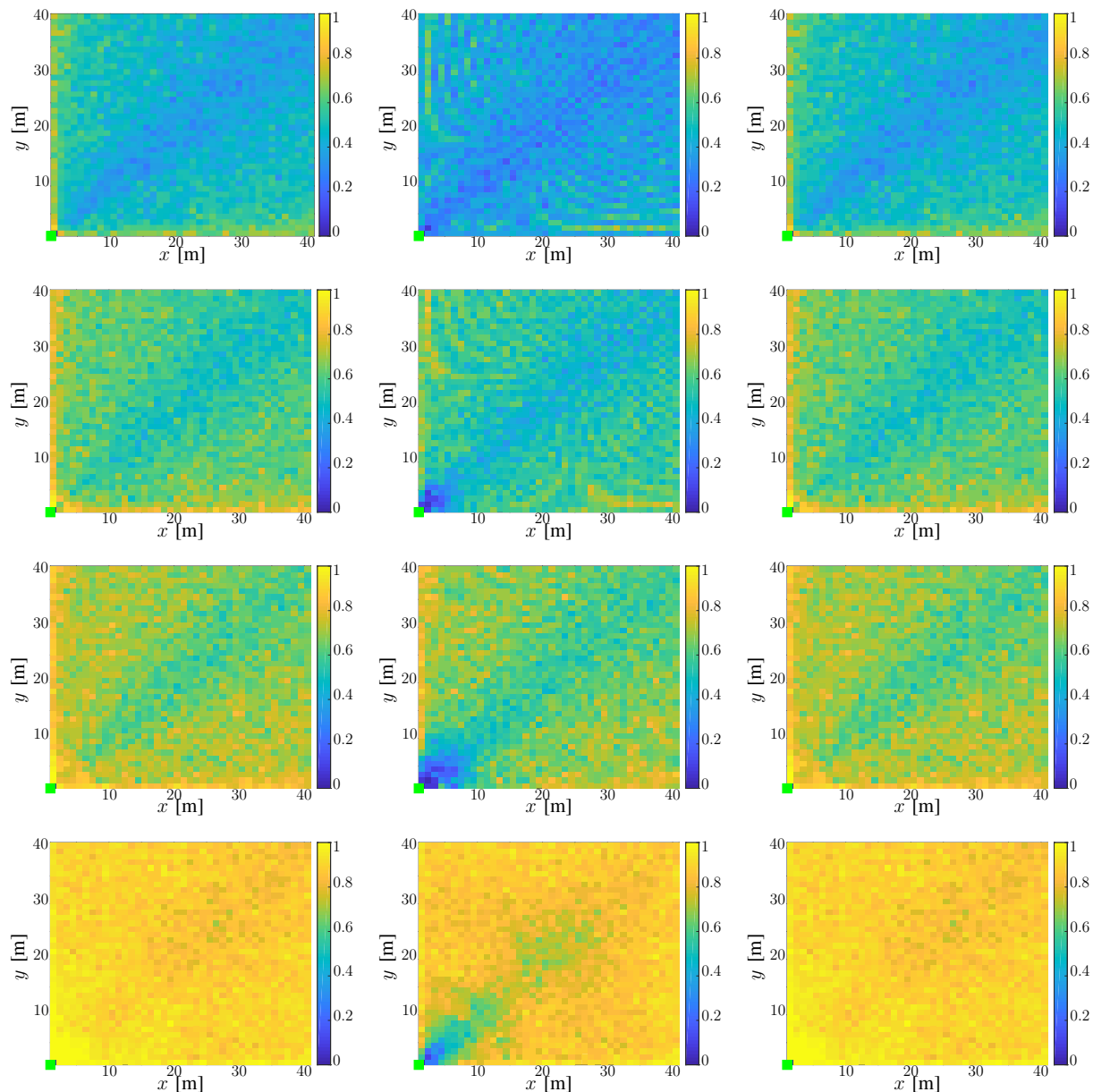


Fig. 13: Coverage rate for interferers distributed as a PPP. Left: no-lens. Middle: NR-lens. Right: R-lens. From top to bottom:  $A_e = 100$ ,  $A_e = 150$ ,  $A_e = 200$  and  $A_e = 10,000$ .

To this purpose, Fig. 13 shows maps for the three architectures (from the left to the right) and for different  $A_e$  (from top to bottom). The value of the points of the map refers to the coverage rate at which  $\text{SIR} > \xi^* = 10$  dB. Indeed, now the impact of  $A_e$  is much more evident as before, and there is a certain improvement when solutions based on R-lens or no-lens are employed, with respect to the NR-lens. The solution with  $A_e = 10,000$ , i.e.,  $A_f = 1 \text{ m}^2$  denotes a robust

interference rejection, even for distances up to 50 m. These results are very promising towards the possibility of realizing multi-user schemes by taking advantage only on the incident spherical wavefront.

## VI. CONCLUSION

In this paper, the possibility to infer the transmitter position from the impinging spherical wavefront curvature at mm-wave has been investigated. This is of crucial importance whenever the TX and the RX are not in far-field, with the advantage that they do not need any ad-hoc synchronization procedure and only a single anchor node is sufficient to estimate the position. To this purpose, we proposed a general model that accounts for the EM processing of the wavefront curvature through a lens (if any), followed by an antenna array scheme.

Then, we analyzed the possibility to employ an EM lens that can be either reconfigurable or fixed, showing how the performance varies when complexity is put in the lens or in the number of employed antennas. In addition, we evaluated also the impact of the multiple-source interference, showing what happens both in a single interference scenario, and in a multiple-interference scenario generated through a PPP. Results show that the considered solutions allow robust source localization using a single receiver, while guaranteeing robustness against multiple-source interference. Furthermore, our framework allows to determine the trade-off between processing the signal at EM or signal level as a function of the target performance and complexity.

Future works will consider also scenarios entailing the presence of multipath or NLOS conditions, where it might become critical to retrieve the position from the spherical wavefront.

## REFERENCES

- [1] M. Z. Win *et al.*, “Network localization and navigation via cooperation,” *IEEE Commun. Mag.*, vol. 49, no. 5, pp. 56–62, 2011.
- [2] M. Z. Win, Y. Shen, and W. Dai, “A theoretical foundation of network localization and navigation,” *Proc. IEEE*, vol. 106, no. 7, pp. 1136–1165, 2018.
- [3] D. Dardari, P. Closas, and P. M. Djurić, “Indoor tracking: Theory, methods, and technologies,” *IEEE Trans. Veh. Technol.*, vol. 64, no. 4, pp. 1263–1278, Apr. 2015.
- [4] A. Guerra, D. Dardari, and P. M. Djurić, “Dynamic radar network of UAVs: A joint navigation and tracking approach,” *IEEE Access*, vol. 8, pp. 116 454–116 469, 2020.
- [5] A. Conti *et al.*, “Soft information for localization-of-things,” *Proc. IEEE*, vol. 107, no. 11, pp. 2240–2264, 2019.
- [6] H. Liu *et al.*, “Survey of wireless indoor positioning techniques and systems,” *IEEE Trans. Syst. Man Cybern. Part C (Applications and Reviews)*, vol. 37, no. 6, pp. 1067–1080, 2007.

- [7] A. Guerra, D. Dardari, and P. M. Djuric, "Dynamic radar networks of UAVs: A tutorial overview and tracking performance comparison with terrestrial radar networks," *IEEE Veh. Technol. Mag.*, vol. 15, no. 2, pp. 113–120, 2020.
- [8] H. Wymeersch *et al.*, "A machine learning approach to ranging error mitigation for UWB localization," *IEEE Trans. Commun.*, vol. 60, no. 6, pp. 1719–1728, Jun. 2012.
- [9] T. Yu and Y. Shen, "Asymptotic performance analysis for landmark learning in indoor localization," *IEEE Commun. Lett.*, vol. 22, no. 4, pp. 740–743, Apr. 2018.
- [10] T. Van Nguyen *et al.*, "Machine learning for wideband localization," *IEEE J. Sel. Areas Commun.*, vol. 33, no. 7, pp. 1357–1380, 2015.
- [11] F. Guidi *et al.*, "Indoor environment-adaptive mapping with beamsteering massive arrays," *IEEE Trans. Veh. Technol.*, vol. 67, no. 10, pp. 10 139–10 143, 2018.
- [12] W. Roh *et al.*, "Millimeter-wave beamforming as an enabling technology for 5G cellular communications: theoretical feasibility and prototype results," *IEEE Commun. Mag.*, vol. 52, no. 2, pp. 106–113, 2014.
- [13] F. Guidi, A. Guerra, and D. Dardari, "Personal mobile radars with millimeter-wave massive arrays for indoor mapping," *IEEE Trans. Mobile Comput.*, vol. 15, no. 6, pp. 1471–1484, Jun. 2016.
- [14] K. Witrisal *et al.*, "High-accuracy localization for assisted living: 5G systems will turn multipath channels from foe to friend," *IEEE Signal Process. Mag.*, vol. 33, no. 2, pp. 59–70, 2016.
- [15] F. Guidi *et al.*, "Joint energy detection and massive array design for localization and mapping," *IEEE Trans. Wireless Commun.*, vol. 16, no. 3, pp. 1359–1371, Mar. 2017.
- [16] Z. Abu-Shaban *et al.*, "Single-anchor two-way localization bounds for 5G mmwave systems," *IEEE Tran. Veh. Technol.*, 2020.
- [17] A. Guerra *et al.*, "A Millimeter-Wave Indoor Backscattering Channel Model for Environment Mapping," *IEEE Trans. Antennas Propag.*, vol. 65, no. 9, pp. 4935–4940, 2017.
- [18] Z. Cheng, Y. Wang, and Y. Shen, "Direct position determination of multiple targets via reduced-dimension beamspace," in *Proc. IEEE Int. Conf. on Commun. Workshops*, May 2017, pp. 1030–1035.
- [19] H. Zhao, L. Zhang, and Y. Shen, "On the optimal beamspace design for direct localization systems," in *Proc. Int. Conf. on Commun. (ICC)*. IEEE, 2018, pp. 1–6.
- [20] N. Garcia *et al.*, "Direct localization for massive mimo," *IEEE Trans. Signal Process.*, vol. 65, no. 10, pp. 2475–2487, 2017.
- [21] L. Taponecco, A. A. D'Amico, and U. Mengali, "Joint TOA and AOA estimation for UWB localization applications," *IEEE Trans. Wireless Commun.*, vol. 10, no. 7, pp. 2207–2217, 2011.
- [22] Y. Shen and M. Z. Win, "Fundamental limits of wideband localization - part I: A general framework," *IEEE Trans. Inf. Theory*, vol. 56, no. 10, pp. 4956–4980, Oct. 2010.
- [23] Y. Wang, Y. Wu, and Y. Shen, "Joint spatiotemporal multipath mitigation in large-scale array localization," *IEEE Trans. Signal Process.*, vol. 67, no. 3, pp. 783–797, Feb 2019.
- [24] —, "On the resolution limits for mimo localization," *IEEE Commun. Lett.*, vol. 23, no. 3, pp. 462–465, Mar. 2019.
- [25] P. Stoica and R. L. Moses, *Spectral analysis of signals*. PRENTICE HALL, 2005, vol. 1.
- [26] S.-F. Chuang, W.-R. Wu, and Y.-T. Liu, "High-resolution AoA estimation for hybrid antenna arrays," *IEEE Trans. Antennas Propag.*, vol. 63, no. 7, pp. 2955–2968, 2015.
- [27] C. Ko and J. Lee, "Performance of ESPRIT and root-MUSIC for angle-of-arrival(aoa) estimation," in *Proc. IEEE World Symp. on Commun. Engineering (WSCE)*, 2018, pp. 49–53.
- [28] A. Guerra, F. Guidi, and D. Dardari, "Single anchor localization and orientation performance limits using massive arrays: MIMO vs. beamforming," *IEEE Trans. Wireless Commun.*, vol. 17, no. 8, pp. 5241–5255, 2018.

- [29] J.-P. Le Cadre, "Performance analysis of wavefront curvature methods for range estimation of a moving source," *IEEE Trans. Aerosp. Electron. Syst.*, vol. 31, no. 3, pp. 1082–1103, 1995.
- [30] B. G. Ferguson and R. J. Wyber, "Wavefront curvature passive ranging in a temporally varying sound propagation medium," in *Proc. MTS/IEEE Oceans. An Ocean Odyssey*, vol. 4, 2001, pp. 2359–2365 vol.4.
- [31] J. P. Delmas *et al.*, "CRB analysis of planar antenna arrays for optimizing near-field source localization," *Signal Process.*, vol. 127, pp. 117 – 134, 2016.
- [32] J. Liang and D. Liu, "Passive localization of mixed near-field and far-field sources using two-stage MUSIC algorithm," *IEEE Trans. Signal Process.*, vol. 58, no. 1, pp. 108–120, Jan. 2010.
- [33] N. Hadaschik, B. Sackenreuter, and M. Faßbinder, "Direct multi-array and multi-tone positioning," in *Proc. IEEE Int. Conf. on Commun. Workshops*, May 2017, pp. 1067–1072.
- [34] M. N. E. Korso *et al.*, "Sequential estimation of the range and the bearing using the Zero-Forcing Music approach," in *Proc. 17th European Signal Process. Conf. (EUSIPCO)*, Aug. 2009, pp. 1404–1408.
- [35] ———, "Deterministic performance bounds on the mean square error for near field source localization," *IEEE Trans. Signal Process.*, vol. 61, no. 4, pp. 871–877, Feb. 2013.
- [36] E. Grosicki, K. Abed-Meraim, and Y. Hua, "A weighted linear prediction method for near-field source localization," *IEEE Trans. Signal Process.*, vol. 53, no. 10, pp. 3651–3660, Oct 2005.
- [37] J.-F. Chen, X.-L. Zhu, and X.-D. Zhang, "A new algorithm for joint range-DOA-frequency estimation of near-field sources," *EURASIP J. Adv. Signal Process.*, vol. 2004, no. 3, p. 105173, Mar 2004.
- [38] K. Deng, Q. Yin, and H. Wang, "Closed form parameters estimation for near field sources," in *Proc. IEEE Int. Symp. on Circuits and Syst.*, May 2007, pp. 3251–3254.
- [39] X. Yin *et al.*, "Scatterer localization using large-scale antenna arrays based on a spherical wave-front parametric model," *IEEE Trans. Wireless Commun.*, vol. 16, no. 10, pp. 6543–6556, Oct 2017.
- [40] P. R. Singh, Y. Wang, and P. Chargé, "Performance enhancement of approximated model based near-field sources localisation techniques," *IET Signal Process.*, vol. 11, no. 7, pp. 825–829, 2017.
- [41] S. Zhang *et al.*, "Spherical wave positioning based on curvature of arrival by an antenna array," *IEEE Wireless Commun. Lett.*, vol. 8, no. 2, pp. 504–507, Apr. 2019.
- [42] N. Vukmirović *et al.*, "Position estimation with a millimeter-wave massive MIMO system based on distributed steerable phased antenna arrays," *EURASIP J. Adv. Signal Process.*, vol. 2018, no. 1, p. 33, 2018.
- [43] ———, "Direct wideband coherent localization by distributed antenna arrays," *Sensors*, vol. 19, no. 20, p. 4582, 2019.
- [44] S. A. Shaikh and A. M. Tonello, "Radio source localization in multipath channels using EM lens assisted massive antennas arrays," *IEEE Access*, vol. 7, pp. 9001–9012, 2019.
- [45] *Samsung 6G White Paper*, 2009 (accessed February 3, 2014). [Online]. Available: <https://cdn.codeground.org/nsr/downloads/researchareas/6G%20Vision.pdf>
- [46] Y. Zeng and R. Zhang, "Millimeter wave MIMO with lens antenna array: A new path division multiplexing paradigm," *IEEE Trans. Commun.*, vol. 64, no. 4, pp. 1557–1571, Apr. 2016.
- [47] Y. Zeng and R. Zhang, "Cost-effective millimeter-wave communications with lens antenna array," *IEEE Wireless Commun.*, vol. 24, no. 4, pp. 81–87, Aug. 2017.
- [48] Y. Zeng, R. Zhang, and Z. N. Chen, "Electromagnetic lens-focusing antenna enabled massive MIMO: Performance improvement and cost reduction," *IEEE J. Sel. Areas Commun.*, vol. 32, no. 6, pp. 1194–1206, 2014.
- [49] F. Guidi, "AOA estimation with EM lens-embedded massive arrays," in *Proc. IEEE Int. Veh. Tech. Conf. (VTC)*, Porto, Portugal, Jun. 2018.

- [50] S. Hu, F. Rusek, and O. Edfors, "Beyond massive MIMO: The potential of data transmission with large intelligent surfaces," *IEEE Trans. Signal Process.*, vol. 66, no. 10, pp. 2746–2758, 2018.
- [51] S. Hu, F. Rusek, and O. Edfors, "Beyond massive MIMO: The potential of positioning with large intelligent surfaces," *IEEE Trans. Signal Process.*, vol. 66, no. 7, pp. 1761–1774, Apr. 2018.
- [52] E. Björnson *et al.*, "Massive mimo is a reality-what is next? Five promising research directions for antenna arrays," *arXiv preprint arXiv:1902.07678*, 2019.
- [53] A. Zappone, M. Di Renzo, and M. Debbah, "Wireless networks design in the era of deep learning: Model-based, AI-based, or both?" *In preparation for submission*, 2020.
- [54] E. Basar *et al.*, "Wireless communications through reconfigurable intelligent surfaces," *arXiv preprint arXiv:1906.09490*, 2019.
- [55] M. Di Renzo *et al.*, "Smart radio environments empowered by reconfigurable ai meta-surfaces: an idea whose time has come," *EURASIP J. Wireless Commun. Netw.*, vol. 2019, no. 1, p. 129, 2019.
- [56] K. Ntontin *et al.*, "Reconfigurable intelligent surfaces vs. relaying: Differences, similarities, and performance comparison," *arXiv preprint arXiv:1908.08747*, 2019.
- [57] H. Li *et al.*, "Wideband transparent beam-forming metadvice with amplitude- and phase-controlled metasurface," *Phys. Rev. Applied*, vol. 11, p. 014043, Jan. 2019.
- [58] B. M. Masini, C. M. Silva, and A. Balador, "The use of meta-surfaces in vehicular networks," *J. of Sensor Actuator Netw.*, vol. 9, no. 1, p. 15, 2020.
- [59] D. Dardari, "Communicating with large intelligent surfaces: Fundamental limits and models," *IEEE J. Sel. Areas Commun.*, vol. 38, no. 11, pp. 2526–2537, 2020.
- [60] A. Elzanaty *et al.*, "Reconfigurable intelligent surfaces for localization: Position and orientation error bounds," *arXiv preprint arXiv:2009.02818*, 2020.
- [61] C. Pfeiffer and A. Grbic, "Millimeter-wave transmitarrays for wavefront and polarization control," *IEEE Trans. Microw. Theory Tech.*, vol. 61, no. 12, pp. 4407–4417, Dec. 2013.
- [62] S. Pandi, C. A. Balanis, and C. R. Birtcher, "Design of scalar impedance holographic metasurfaces for antenna beam formation with desired polarization," *IEEE Trans. Antennas Propag.*, vol. 63, no. 7, pp. 3016–3024, Jul. 2015.
- [63] A. Silva *et al.*, "Performing mathematical operations with metamaterials," *Science*, vol. 343, no. 6167, pp. 160–163, 2014.
- [64] L. Di Palma *et al.*, "Circularly-polarized reconfigurable transmitarray in Ka-band with beam scanning and polarization switching capabilities," *IEEE Trans. Antennas and Propag.*, vol. 65, no. 2, pp. 529–540, Feb. 2017.
- [65] S. V. Hum and J. Perruisseau-Carrier, "Reconfigurable reflectarrays and array lenses for dynamic antenna beam control: A review," *IEEE Trans. Antennas Propag.*, vol. 62, no. 1, pp. 183–198, Jan. 2014.
- [66] D. Dardari and F. Guidi, "Direct position estimation from wavefront curvature with single antenna array," in *Proc. 8th Int. Conf. on Localization and GNSS (ICL-GNSS)*, 2018, pp. 1–5.
- [67] A. Guerra *et al.*, "Near-field tracking with large antenna arrays: Fundamental limits and performance," *arXiv preprint arXiv:1902.02647*, 2019.
- [68] P. Nepa and A. Buffi, "Near-field-focused microwave antennas: Near-field shaping and implementation," *IEEE Antennas Propag. Mag.*, vol. 59, no. 3, pp. 42–53, 2017.
- [69] J. Yang *et al.*, "3-D position and velocity estimation in 5G mmwave CRAN with lens antenna arrays," in *Proc. IEEE 90th Veh. Technol. Conf. (VTC2019-Fall)*, 2019, pp. 1–6.